Magnetometer-Free Orientation Estimation Using Multiple Inertial Measurement Units

T. I. Edridge

TUDelft
Delft
University of
Technology

Magnetometer-Free Orientation Estimation Using Multiple Inertial Measurement Units

MASTER OF SCIENCE THESIS

For the degree of Master of Science in Systems and Control at Delft University of Technology

T. I. Edridge

October 5, 2020

Faculty of Mechanical, Maritime and Materials Engineering (3mE) · Delft University of Technology

Abstract

Higher-grade Inertial Measurement Units (IMUs) provide a better estimation of the orientation but are more expensive than lower-grade IMUs. The increase in availability and affordability of lower-grade IMUs over the last few years has provided an alternate solution: combine multiple lower-grade IMUs to increase sensor accuracy at low cost. Existing literature has already shown the advantages of multiple IMUs. One advantage is a better estimation of linear and rotational motion. Another advantage is Fault Detection and Isolation (FDI) from component redundancy. However, existing literature is confined to a set of configurations that are impractical (platonic solids) or small (arrays). In this thesis, we focus on combining FDI with a better estimation of linear and rotational motion and further improve FDI by changing the IMU configuration from an array to scattered placement of IMUs. First, we show in a Monte Carlo simulation that because of the array configuration, the angular velocity and angular acceleration covariance decrease proportionally with the number of accelerometers used rather than quadratically, which is theoretically possible. We also reveal that the angular velocity covariance can compete with a higher-grade IMU, although the specific force covariance is worse. Second, we propose a novel FDI method to reject disturbances. As a proof of concept for real-life implementation, we tested FDI on a simulated human arm with three configurations. The first with lower-grade IMUs scattered across the arm. The second and third with a lower-grade IMU array and a single higher-grade respectively in the middle of the arm. A disturbance was applied that diminished over the length of the arm. The configurations have a $1.00°$, $5.72°$ and $2.06°$ yaw error respectively after the disturbance. In conclusion, we show that combining multiple IMUs improves accuracy and for certain applications, depending on the configuration Multiple lower-grade IMUs can be desirable. The practical limitations are discussed in this thesis.

Table of Contents

List of Figures

List of Tables

Acknowledgements

I would like to thank my supervisor dr. ir. M. Kok for her time and assistance during the thesis. I would also like to thank Frida, Evan, Bart, Daan and Stefan for your helpful comments and sharing your insights during the bi-weekly meetings.

Chapter 1

Introduction

In Section 1-1 of this Chapter the motivation of the research is shown, as well as the research questions that guide this Thesis. Afterwards, in Sections 1-2 and 1-3 the existing work regarding Multiple IMU fusion and Fault Detection and Isolation are discussed. The contributions of this Thesis is shown thereafter is Section 1-5. This Chapter ends on introducing the outline of the thesis in Section 1-6.

herschrijven als 't af is

1-1 Background Research motivation

Inertial Measurement Units (IMUs) are electronic devices used for measuring the movement of an object or person also known as motion capture [4]. Over the last decades, Micro-Electromechanical System (MEMS) technology has revolutionized the IMU industry [5], making them ubiquitous [3]. MEMS IMUs (see Figure 1-1 for an example) are lightweight, cheap and small-sized [6] which has made them preferable over the most common alternative method of motion capture, optical motion capture [7] which is limited in practicality and affordability [8]. This has increased use of MEMS IMUs in motion capture for varying fields [4, 5]. Some examples are bio-mechanics, video games, sports and navigation.

Figure 1-1: Xsens [1] MTw Awinda wearable MEMS IMU containing a gyroscope and an accelerometer.

A MEMS IMU consists of two different tri-axial sensors. One is the gyroscope, which measures the angular velocity. The gyroscope measurement, is integrated to find the orientation, but when corrupted by a bias, the error will accumulate, also known as drift from the true orientation [5]. The other is the accelerometer, which measures the gravity vector and the linear acceleration, also known as the specific force. The accelerometer reveals information on the direction of the gravity vector, which gives information on the roll (around the x-axis) and pitch (around the y-axis) angle. This information can be used to compensate for the drift around the roll and pitch angle. However, the accelerometer provides reveals no information on the rotation of the gravity vector, leaving the yaw (around the z-axis) angle uncompensated for. Frequently, a magnetometer is added to compensate for the drift around the yaw angle. However, magnetometers are prone to disturbances in indoor environments [8]. This makes the use of magnetometers unfavourable.

MEMS IMUs come in different grades, where the higher-grade IMUs have higher measurement accuracy and provide more stable readings [9] (Note that the terms higher- and lower- are relative and an example of each will be given later). The drift is generally worse for lower-grade IMUs as higher-grade IMUs rely on higher angular velocity accuracy and better bias stability [1]. Bias stability is one of the main sources of error [10]. This results in precise calibration in a factory being more effective for higher-grade IMUs than lower-grade IMUs [11]. As a result, calibration for cheaper IMUs is usually left out. Despite the higher accuracy of higher-grade MEMS IMUs, their high costs limit their use in many applications.

Over the last years, the prices of lower-grade IMUs have decreased and the availability has increased [12]. This has provided a potential solution to increase the orientation estimate: combine multiple lower-grade IMUs to increase motion accuracy at low cost . Combining multiple sensors together, also known as Sensor Fusion, forms a synthetic IMU which shows high performance-price to ratio [13]. The general idea of a Synthetic IMU is to mimic higher-grade IMU capabilities, but there is more potential to be gained than just fusion multiple sensors [3]. Two important additional benefits of using Multiple IMUs are direct estimation

add costs

of the angular acceleration and Fault Detection and Isolation (FDI) based on component redundancy. This gives the overall goal of this thesis:

How can multiple IMUs be used to improve orientation estimation?

Before more detailed research questions can be formulated, we first will look into existing work on Multiple IMUs. The fusion of Multiple IMUs is discussed primarily followed by FDI in Sections 1-2 and 1-3 respectively.

1-2   Existing work on fusion of Multiple IMUs

The theory of using Multiple IMUs is not new, publications began appearing around the 1960s and has found renewed interest in the last two decades due to the new MEMS technology [3] (see [3] for a detailed literature review on IMU arrays). The main focus of using Multiple IMUs in for orientation estimation is the increased accuracy and reliability in estimating linear and rotational motion [3]. As previously mentioned, the gyroscopes measure the angular velocity and the accelerometer measure the specific force. By averaging out these measurements, more accurate estimates of the angular velocity and specific force can be attained. While averaging is computationally efficient, more accurate estimates are attainable [14]. This is because accelerometers are also affected by rotational motion, both the angular velocity and the angular acceleration are measured by the accelerometer. The angular velocity and the angular acceleration induces a Centrifugal and Euler force respectively. The forces measured by the accelerometer are shown in Figure 1-2. By recognizing the rotational forces the accelerometers can provide information on the angular velocity, allowing more accurate angular velocity estimates. Additionally, the angular acceleration can now be estimated directly as well. Because the rotational motion is now separated from the accelerometer measurements, a better estimate on the specific force is attainable, as the rotational motion could be considered a source of error.
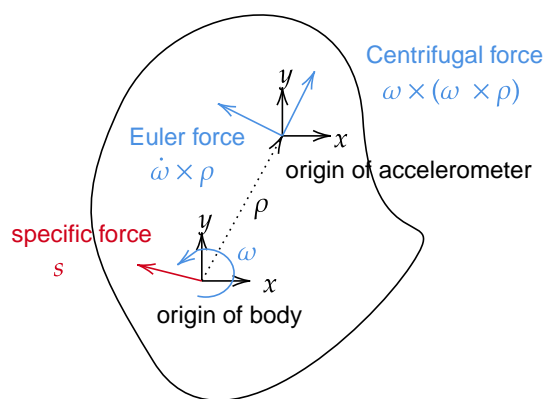
Figure 1-2: Rigid body experiencing linear (red) and rotational (blue) motion, resulting in a specific force s, Centrifugal force $\omega \times (\omega \times \rho)$ and Euler force $\dot{\omega} \times \rho$. The angular velocity is denoted by ρ, angular acceleration is denoted by $\dot{\omega}$ and relative position of the accelerometer by ρ.

Research on fusing Multiple IMUs is mostly limited to an array configuration, an example of an IMU array can be seen in Figure 1-3. The relative locations of the accelerometers on the IMU array are small $\approx 5mm$. The downside, however, is that the relative locations of the accelerometers are in fact small. The advantage of an IMU array is that the IMU array is practical in use and the locations are fixed with respect to each other. As shown in [14], the accelerometer provides more information on the angular velocity and the angular acceleration when the distance between sensors increases. More specifically, the covariance of the angular velocity and the angular acceleration decreases proportionally with the distance between accelerometers squared.
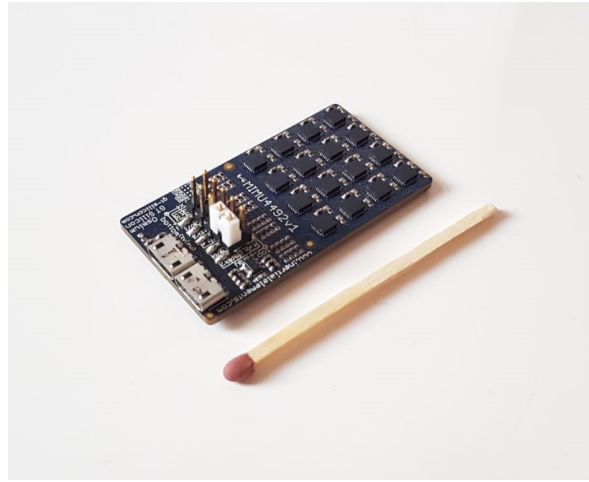
Figure 1-3: MIMU4844 IMU array from Inertial Elements [2] containing 32 accelerometers, 32 gyroscopes and 32 magnetometers.

Arrays can be divided into two types: accelerometer and gyroscope arrays or IMU arrays and gyro-free arrays or accelerometer-only arrays. Accelerometer-only arrays are generally used in high dynamic environments [3], as it can be shown that accelerometers provide better accuracy at higher dynamics [14], for example in crash tests for vehicles [3]. The downside of using accelerometer-only arrays is that the angular velocity can be estimated up to a sign ambiguity. A lot of different methods have been introduced to resolve the sign ambiguity, see [15] for an overview. Accelerometer-only arrays are usually used in high-dynamic environments as the accuracy on the estimation of the angular velocity is more accurate with higher dynamics [14]. IMU arrays are more suitable for lower dynamic environments [3] such as motion capture [5]. This is because the gyroscopes provide a good estimation on the angular velocity.

A Maximum Likelihood (ML) approach for IMU arrays to estimate the linear and rotational motion the specific force, angular velocity and angular acceleration of a rigid body was presented by Skog et al. in [14]. As an extension on this work, [16] showed improvements that can be made using the angular acceleration as a motion model. Resulting in a Maximum A Posteriori (MAP) estimate of the angular velocity. This resulted in higher accuracy of the angular velocity and allows for the extension towards accelerometer-only arrays. The theory presented by Skog et al. was also extended in [8], where the authors used a two-step attitude

integration architecture [8] by [17] which allows for computationally cheaper estimations. An IMU array of 8 IMUs was compared to a single IMU and the peak estimation error was reduced by a factor of 2.5.

1-3   Existing work on Fault Detection and Isolation

Fault Detection and Isolation (FDI) has been a research topic since the early the early days of Inertial Navigation [18]. The term Inertial Navigation is estimating the position, velocity and orientation of an object using IMUs. The focus was on building fail-safe systems, where fail-safe denotes the ability to identify and isolate faulty sensors [18]. Recently, with the rise of cheaper MEMS IMUs, interest in FDI application for IMU has increased. Commonly, the application of FDI is combined with additional measurements such as GPS. GPS, however, has poor performance in indoor and rural environments [19], this makes the use of GPS for indoor applications undesirable.

The majority of the research on FDI focuses on the parity space. The parity space is a method used for FDI based on either analytical or component redundancy. Analytical redundancy refers to the ability to link past states with current states using a mathematical model. This type of redundancy is applied when using a single IMU. Component redundancy refers to having multiple IMUs, where the measurements can be tested against one another. Besides this difference, the method and the application of the parity space method .

Research has been done on optimal configurations using IMUs, see for example [20, 21, 22, 23, 24, 6, 25]. The results show that two types of configurations are optimal in detecting faults: the platonic solids and the half cones which are shown in Figure 1-4. The problem with such configurations, however, is twofold. The first problem is that the costs of such a special configuration outweigh the costs of adding more sensors [26], which would have the same results. The second problem is that placing sensors in such a way is usually impractical. For example, placing sensors on a human body part would not result in the optimal configuration.

The previous work on the parity space using component redundancy, see e.g. [18, 27, 23], assume that the accelerometer only measures the specific force. While this assumption may hold in some cases, low angular motion and closely placed accelerometers. For conditions where the angular motion high and accelerometers are placed further away, this will result in unmodeled errors [28]. The angular acceleration can be found by taking the angular velocity time derivative, however, this considered to be unreliable as this induces large errors on the angular acceleration estimate. In some accounts these states were added, e.g. [28, 26], however, their works do not make use of the parity space method.
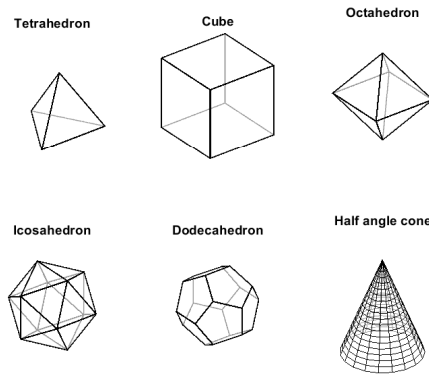
Figure 1-4: Platonic solids and a half angle cone.

1-4   Research Questions

Restating the overall goal of this thesis:

How can multiple IMUs be used to improve orientation estimation?

With the knowledge based on previous work we can now ask more specific questions

How can multiple lower-grade IMUs compare against a higher-grade IMU?   It was shown in [14] that Multiple IMUs can be fused into a single Synthetic IMU. It was shown that at higher angular velocities, the accuracy of the angular velocity increases. It was also shown that with more distance between accelerometers, the angular velocity accuracy increases. Additionally, a direct estimation of the angular acceleration becomes attainable. The angular acceleration was used in [16] as a motion model so that the accuracy can be even further increased. How do the angular velocity covariance and the specific force covariance compare against a higher-grade IMU.

How can the component redundancy of IMUs be used to reject disturbances?   By making use of Multiple IMUs, the amount of information available becomes redundant at every time step. The IMUs can be compared to each other to determine if IMUs are corrupted by faults. If a sensors is faulty, it can be isolated until the fault has disappeared. Previous work has focused on specific configurations, however, other configurations might provide useful information. If for example, IMUs were scattered along the length of a human arm and a disturbance is applied that dissipates along the length of this arm, can a scattered configuration reject the disturbance when an IMU array cannot?

How can the rotational motion be included in the parity space method?   Previous accounts on the parity space method assume that the accelerometer measure the specific force and no angular motion. This can give good results a low angular motion and short distances between the accelerometers. However, if the angular velocity gets higher or the distance

between accelerometers increases, the angular motion will create larger differences between the measurements. This may cause the parity space method to false identify faulty sensors. By making use of the formulation shown in [16] base on the works in Skog et al. the angular motion can be taken into account.

1-5 Contributions of the Thesis

This thesis aims to analyze how Multiple IMUs can be used to obtain better estimates of orientation estimates. The contribution of this thesis is threefold. Firstly, based on the works in [14] the covariance analysis is extended towards a real IMU array such that more realistic covariance estimates are shown. Secondly, by making use of several motion priors, different Multiple lower-grade IMU configurations are compared to each other and a higher-grade IMU. Thirdly, the parity space method as an extension on the work in [14] is developed. Note that the parity space method has been used repeatedly, to the knowledge of the writer this is the first time it is used as an extension on the works in [14].

Deze helemaal herschrijven als resultaten gefixt zijn

1-6 Outline of the Thesis

In Chapter 2, it is shown how a navigation solution can be found using a single IMU. Afterwards, in Chapter 3, it is shown how measurements can be fused into a Synthetic IMU. It becomes apparent how much information can be obtained and how it can be combined with Chapter 2 to obtain a navigation solution. Subsequently, in Chapter 4 results are shown on how much information can be obtained and different setups are compared against a high-grade IMU. In Chapter 5, it is discussed how component redundancy can be used to Detect and Isolate Faulty sensors. It is also shown how this can be integrated with the theory presented in Chapters 2 and 3. This is then put to the test in Chapter 6 in which the novel parity space is simulated and tested. Finally, in Chapter 7, the results are discussed, further recommendations are given and a conclusion is drawn.

Chapter 2

Single IMU Inertial Navigation

This chapter introduces the fundamental basics for orientation estimation using accelerometers and gyroscopes. In this Chapter, a Single IMU is used to find the orientation estimation. It will be shown later in Chapter 3 how a Synthetic IMU can be fused from Multiple IMUs. The Synthetic IMU can take the place of the single IMU to find the orientation estimation. Section 2-1 introduces the coordinate frames necessary to express the orientation. Afterwards, in Section 2-2, different motion models are introduced. Thereafter, in Section 2-3 filtering is introduced, where the measurements used to estimate the orientation. In Section 2-4 calibration is introduced for the gyroscope and accelerometer. Finally, in Section 2-5, the previous sections are brought together into a single Inertial Navigation Solution scheme.

2-1 Describing orientation

The orientation and position of a body in a 3-D space can be represented in different ways. However, in order for these results to have any meaning, coordinate frames can be introduced to describe the relative change from an initial position. The coordinate frames are shown first in the section after which the relevant orientation parameterizations are discussed.

2-1-1 Coordinate frames

The orientation estimates of a body in a space can hold can hold many different solutions. It is important to identify which frames play an important role in describing these estimates. The relevant frames here are defined as

- Sensor frame s - frame in which the measurement is done by an individual sensor.

- Body frame b - frame attached to the center of mass of the body of which the position and orientation is to be estimated.

- Navigation frame n - frame in which the body moves.

The measurements take place directly in the sensor frame. These measurements are fused together into a single state vector in the body frame. This state vector can then be used to find a navigation solution in the navigation frame.

2-1-2   Orientation Parameterization

The orientation of a rigid body can be parameterized in different ways. The relevant orientation parameterizations are shown below. Additional information on other orientation parameterizations can be found in Appendix A-1. These different parameterizations can be used interchangeably as they can be expressed in terms of the SO(3) group, which describes the group of all rotations in $\mathbb{R}^3$. The SO(3) group itself is in the matrix Lie group and the SO(3) group has the following properties [29], where R is a rotation matrix

$$R^T = R^{-1}, \quad R^T R = \mathcal{I}_3, \quad \det(R) = 1. \tag{2-1}$$

Rotation matrices   A rotation matrix describes the relative rotation of a fixed-length vector from one coordinate system to another coordinate system, in this case from s to b. The indices of the matrix in equation (2-2) contain the cosine of the angle between the new axis and the old axis, where the first superscript denotes coordinate system s and the second superscript denotes coordinate system b [30]. A rotation matrix that describes the rotation $x^b = R^{bs}x^s$ can be written as

$$\underbrace{\begin{bmatrix} x_1^b \\ x_2^b \\ x_3^b \end{bmatrix}}_{x^b} = \underbrace{\begin{bmatrix} C_{x_1^b, x_1^s} & C_{x_1^b, x_2^s} & C_{x_1^b, x_3^s} \\ C_{x_2^b, x_1^s} & C_{x_2^b, x_2^s} & C_{x_2^b, x_3^s} \\ C_{x_3^b, x_1^s} & C_{x_3^b, x_2^s} & C_{x_3^b, x_3^s} \end{bmatrix}}_{R^{bs}} \underbrace{\begin{bmatrix} x_1^s \\ x_2^s \\ x_3^s \end{bmatrix}}_{x^s}. \tag{2-2}$$

The rotation matrix also has some unique properties that must be upheld to describe a rotation. A rotation matrix is a unique way of describing a rotation, where all nine entries of the rotation matrix describe a different part of the rotation. the properties of the rotation matrix are that given by equation (2-1).

Quaternions   Unit quaternions provide another approach on how to parameterize rotations. This, 4-dimensional representation has no feasible physical interpretation but is known for its applicability in Gaussian filters such as the Kalman filter. The main reason for this is that the unit quaternion is not prone to wrapping, unlike the other parameterizations and gives a non-singular orientation [29]. The quaternion, however, is non-unique as $-q$ and q describe the same orientation. Furthermore, the unit quaternion is said to be in the group $\mathbb{S}^3$ under the following conditions

$$q = \begin{bmatrix} q_0 & q_1 & q_2 & q_3 \end{bmatrix}^T = \begin{bmatrix} q_0 \\ q_v \end{bmatrix}, \qquad q \in \mathbb{R}^4, \qquad ||q||_2 = 1. \tag{2-3}$$

The quaternion multiplication $\odot$ is denoted by

$$p \odot q = \begin{bmatrix} p_0 q_0 - p_v \cdot q_v \\ p_0 q_v + q_0 p_v + p_v \times q_v \end{bmatrix}. \tag{2-4}$$

Orientation deviations   Orientation deviations are closely related to the previously discussed orientation parameterizations as the rotation can be described as a linearization point around the quaternion or rotation matrix and an orientation deviation around this point [5]. This property can be used in the Extended Kalman Filter (EKF) and will be shown in section 2-3. The rotation quaternion using orientation deviations can be defined as

$$q_k^{nb} = \exp_q(\frac{\bar{\eta}_t^n}{2}) \odot \tilde{q}_k^{nb}. \tag{2-5}$$

Where the mapping from quaternion to SO3 with the approximations based on the small angle theorem are denoted as

$$\exp_q(\bar{\eta}) = \begin{bmatrix} \cos ||\eta||_2 \\ \frac{\eta}{||\eta||_2} \sin ||\eta||_2 \end{bmatrix}, \qquad \exp_q(\eta) \approx \begin{bmatrix} 1 \\ \eta \end{bmatrix}. \tag{2-6}$$

2-2   Motion models for orientation estimation

To determine the orientation of a rigid body use can be made of motion models and measurement models. These can be described into a state-space model which in turn can be used in a Kalman Filter as will be shown later in Section 2-3. The measurements are sampled at a certain frequency at which the motion models are Euler discretized. The measurements are assumed to take on additive Gaussian white noise and a bias.

2-2-1   Discretized motion models

For orientation estimation the gyroscopes provide direct measurements of the angular velocity. Combing these and by making use of quaternions, the attitude can be expressed as (where $\odot$ is the quaternion multiplication operator defined in equation (A-12)) with its Euler discretization [5] gives the following update equations

$$\omega_{k+1}^b = \omega_k^b + e_{\omega,k}, \tag{2-7a}$$

$$q_{k+1}^{nb} = q_k^{nb} \odot \exp_q(\frac{T}{2}\omega_k^b). \tag{2-7b}$$

Where q_k^{nb} denotes the quaternion, T denotes the sampling time and ω_k^b denotes the angular velocity. Furthermore, $e_{\omega,k} \sim \mathcal{N}(0, \Sigma_\omega)$ is Gaussian white noise.

2-2-2   Measurement models

Micro-Electromechanical System (MEMS) Inertial Measurement Units (IMUs) are readily available and provide angular velocity and linear acceleration measurements. These measurements, however, are corrupted by bias and noise [10]. For better estimations it becomes key to account for these biases as these errors will accumulate when integrating [10]. For this a measurement model is needed. Additionally, for the accelerometers in pose estimation, one would like to account for the gravity vector as well.

Gyroscope measurement model   The gyroscope, measuring the angular velocity of the body, which is independent on its location is given by

$$y_{\omega,k} = \omega_k^s + b_{\omega,k}^s + e_{\omega,k}^s. \tag{2-8}$$

The noise vector $e_{\omega,k}^s$ can be modeled as Gaussian white noise with only diagonal entries and is assumed to be modeled as $e_{\omega,k}^s \sim \mathcal{N}(0, \Sigma_\omega)$. The bias, denoted by $b_{\omega,k}^s$ is slowly time-varying and can be modeled as constant or as a random walk model given by

$$b_{\omega,k+1}^s = b_{\omega,k}^s + e_{b_\omega,k}^s, \tag{2-9}$$

depending on the duration time of the experiment [5]. Furthermore, the assumptions are often made that the earth's rotation and that the navigation frame have negligible effect on the measurements [5].

Accelerometer measurement model   The accelerometer which measures the specific force has a measurement model which can be denoted by

$$y_{a,k} = s_k^s + b_{a,k}^s + e_{a,k}^s. \tag{2-10}$$

The noise term $e_{a,k}^s \sim \mathcal{N}(0, \Sigma_a)$ can be modeled as Gaussian white mean with only diagonal entries. Furthermore, the assumption here is made that the Coriolis acceleration is negligible [5]. The bias, being similar to the bias in the gyroscope can again be modeled as constant or slowly time-varying as a random walk model given by

$$b_{a,k+1}^s = b_{a,k}^s + e_{b_a,k}^s. \tag{2-11}$$

The specific force can be recast into terms of a gravity vector and linear acceleration which results into the final measurement model of

$$y_{a,k} = \underbrace{(a_k^s - R_k^{sn} g^n)}_{s_k^s} + b_{a,k}^s + e_{a,k}^s, \tag{2-12}$$

however, in some applications a good enough approximation would be to ignore the linear acceleration and only take the gravity vector into account [5]. This results in the simplified measurement model of

$$y_{a,k} = -R_k^{sn} g^n + b_{a,k}^s + e_{a,k}^s. \tag{2-13}$$

2-2-3   Orientation estimation

Using the previously mentioned motion models and the previously mentioned algorithms one can combine these to estimate orientation. The assumptions can be made that the rotation of the earth and the Coriolis acceleration are negligible [5]. An assumption can be made that the linear acceleration measured by the accelerometer is almost zero [5], which results in only the gravity vector having effect.

$$q_{k+1}^{nb} = q_k^{nb} \odot \exp_q(\frac{T}{2}(y_{\omega,k} - b_\omega - e_{\omega,k})), \tag{2-14a}$$

$$y_{a,k} = -R_k^{bn} g^n + e_{a,k}. \tag{2-14b}$$

2-3   Using filtering for orientation estimation

Now that the motion models and the measurements models are discussed they need to be fused together. This can be done via smoothing or filtering, the former approach gives better state estimates but is computationally more heavy [5]. Filtering is less accurate but faster can be used on-line. These features, make filtering an attractive solution for longer data sets and for many sensors. For this reason, the Extended Kalman Filter (EKF) will be discussed which forms a basis for the Multiplicative Extended Kalman Filter (MEKF). How a prior is obtained not discussed, the reader is referred to [5].

2-3-1   Extended Kalman Filter

The Kalman Filter (KF) is an unbiased minimum-variance estimator gives a one-step-ahead prediction of the filtered state estimate [31]. The Extended Kalman Filter (EKF) is an adaptation on the KF that allows for estimation of non-linear functions. The EKF works under the assumption that noise is additive and that both process noise Q and measurement noise R are distributed as Gaussian zero-mean with constant or time-varying co-variance [5]. The EKF is presented in [5] and is as follows. The EKF is a recursive algorithm that performs two updates, one being a time update where the next state $x_{k+1|k}$ and its co-variance $P_{k+1|k}$ are estimated. The algorithm is shown in Algorithm 1.

Algorithm 1: Extended Kalman Filter

compute the prior and set initial values;
for $k = 2 : N$ **do**
  Time update;

$$\hat{x}_{k+1|k} = f_k(\hat{x}_{k|k}, u_k), \qquad (2\text{-}15a)$$
$$P_{k+1|k} = F_k P_{k|k} F_k^T + G_k Q G_k^T. \qquad (2\text{-}15b)$$

  Measurement update;

$$\hat{x}_{k+1|k+1} = \hat{x}_{k+1|k} + K_{k+1}\epsilon_{k+1}, \qquad (2\text{-}16a)$$
$$P_{k+1|k+1} = P_{k+1|k} - K_{k+1}S_{k+1}K_{k+1}^T, \qquad (2\text{-}16b)$$

end

Where the terms F_k and G_k are linearized as defined as

$$F_k = \frac{\partial f_k(x_k, u_k, e_k)}{x_k}\Big|_{e_k=0, x_k=\hat{x}_{k|k}}, \quad G_k = \frac{\partial f_k(x_k, u_k, e_k)}{e_k}\Big|_{e_k=0, x_k=\hat{x}_{k|k}}, \qquad (2\text{-}17)$$

and ϵ_{k+1}, S_{k+1} and K_k are defined as

$$\epsilon_{k+1} = y_{k+1} - \hat{y}_{k+1|k}, \quad S_{k+1} = H_{k+1}P_{k+1|k}H_{k+1}^T + R, \quad K_{k+1} = P_{k+1|k}H_{k+1}^T S_{k+1}^{-1}, \quad (2\text{-}18)$$

and $\hat{y}_{k+1|k}$ and H_k are defined as

$$\hat{y}_{k+1|k} = h(\hat{x}_{k+1|k}), \qquad H_k = \frac{h_{k+1}(x_{k+1})}{\partial x_{k+1}}\big|_{x_{k+1}=\hat{x}_{k+1|k}}. \qquad (2\text{-}19)$$

2-3-2   Multiplicative Extended Kalman Filter

One of the useful adaptations on the EKF is the MEKF, which is designed for orientation estimation. The MEKF uses orientation deviations described in Section 2-1-2 instead of unit quaternions described in Section 2-1-2. This is advantageous as orientation deviations are computationally more attractive than quaternions due to their lower-dimensional state [5, 32]. When using unit quaternions in the EKF one has to normalize the resulting solution for it to represent a pure rotation, creating an additional step compared to the regular EKF. This is because the orientation deviation $\hat{\eta}_k^n$ is non-zero and has to be reset [5]. The orientation deviation can be seen as an error between the truth and the estimate [33] in terms of an angle-axis representation. The MEKF described in [5] is shown in the Algorithm 2.

Algorithm 2: Multiplicative Extended Kalman Filter

compute the prior and set initial values;
for $k = 2 : N$ **do**

Time update;

$$\hat{q}_{k|k-1}^{nb} = \hat{q}_{k-1|k-1}^{nb} \odot \exp_q(\frac{T}{2} y_{\omega,k-1}), \qquad (2\text{-}20\text{a})$$

$$P_{k|k-1} = P_{k-1|k-1} + G_{k-1}QG_{k-1}^T. \qquad (2\text{-}20\text{b})$$

Measurement update;

$$\hat{\eta}_k^n = K_k \epsilon_k, \qquad (2\text{-}21\text{a})$$

$$\tilde{P}_{k|k} = P_{k|k-1} - K_k S_k K_k^T. \qquad (2\text{-}21\text{b})$$

Relinearize;

$$\hat{q}_{k|k}^{nb} = \exp_q(\frac{\hat{\eta}_k^n}{2}) \odot \tilde{q}_{k|k-1}^{nb}. \qquad (2\text{-}22)$$

end

Where ϵ_k, K_k and S_k are defined in equation (2-18). G_k, y_k, $\hat{y}_{k|k-1}$ and H_k are defined as

$$G_{k-1} = T\tilde{R}_{k|k-1}^{nb}, \qquad (2\text{-}23\text{a})$$

$$y_k = y_{a,k}, \qquad (2\text{-}23\text{b})$$

$$\hat{y}_{k|k-1} = -\tilde{R}_{k|k-1}^{bn}g^n, \qquad (2\text{-}23\text{c})$$

$$H_k = -\tilde{R}_{k|k-1}^{bn}[g^n\times]. \qquad (2\text{-}23\text{d})$$

2-4   IMU Calibration

MEMS inertial sensors as mentioned are prone to systematic errors and biases. Even though these bias errors can be precisely calibrated by the manufacturers, this is usually rather expensive [11] and these errors may change over time [10]. For these lower quality sensors, cross-axis errors can take place which has to be compensated for leading to three additional parameters [34]. Additionally, when multiple sensors are placed on a rigid body, the relative orientation between sensors becomes important, again leading to three additional parameters to be estimated [11]. The accuracy of these sensors is therefore highly dependent on the calibration techniques to remove these biases and systematic errors [35].

2-4-1   Gyroscope calibration

Gyroscopes are rather easy to calibrate, this is because their measurements are independent of any geometric configuration and when lain on a flat surface, the measured rotational velocity should be zero. This is illustrated by the measurement model as shown in (2-24). Furthermore, the co-variance can be determined as the deviation of the measurements. The measurement model of the gyroscope

$$y_{\omega,k} = \omega_k + b_{\omega,k} + e_{\omega,k}, \tag{2-24}$$

is assumed to be corrupted by a slowly time-varying $b_{\omega,k}$ bias and zero-mean white noise denoted by $e_{\omega,k} \sim \mathcal{N}(0, \Sigma_\omega)$ [5]. Under the assumption that the gyroscope is properly calibrated, the axes are assumed to have independent measurements and as such, the co-variance Σ_ω can be modeled as a diagonal matrix which takes the form of

$$\Sigma_\omega = \begin{bmatrix} \sigma_{\omega,x}^2 & 0 & 0 \\ 0 & \sigma_{\omega,y}^2 & 0 \\ 0 & 0 & \sigma_{\omega,z}^2 \end{bmatrix}. \tag{2-25}$$

By placing the gyroscope on a flat surface ensures that the only rotation that the gyroscope undergoes is due to the earth's rotation. However, the magnitude of this rotation is insignificant compared to sensor noise and can thus be assumed to be approximately zero [36].

When the gyroscope lies flat on the table for a period of time, the biases can be found as the mean of the data and the co-variance can be found as the standard deviation from this mean [35], which can be modeled as in (2-24).

2-4-2   Accelerometer calibration

Contrary to gyroscope calibration, accelerometer calibration is not as straightforward. The calibration technique described, taken from [35, 11, 37, 36] does not require the accelerometer to be placed in specific orientations. This calibration method requires the accelerometer to be rotated, slowly, in as many directions as possible. The basic principle of the calibration

technique relies on the assumption that the local gravity field is constant. It is also important to note that accelerometer calibration is often neglected for orientation estimation. This is because the approximation is made that the gravity vector is equal to the specific force.

The accelerometer measurement model,

$$y_{a,k} = s_k^s + b_a^s + e_{a,k}^s, \tag{2-26}$$

where b_a, k is the bias and $e_{a,k}$ is Gaussian white noise denoted by $e_{a,k} \sim \mathcal{N}(0, \Sigma_a)$ similar to the gyroscope noise. The measurement model can be adapted to include cross-axis interference and non-orthogonal axes, which makes for 9 parameters to be estimated [34]. This results in the following uncalibrated measurement model, under the assumption that linear acceleration is approximately zero.

$$y_{a,k} = -DR_k^{sn}g^n + b_a^s + e_{a,k}^s. \tag{2-27}$$

The rotation matrix R_k^{sn} denotes the orientation of the sensor. The matrix D models the errors in cross-axis interference, inter-sensor misalignment and non-orthogonal axes, which can be decomposed into a scaling matrix K and a misalignment matrix T. These take the form of

$$D = \underbrace{\begin{bmatrix} k_x & 0 & 0 \\ 0 & k_y & 0 \\ 0 & 0 & k_z \end{bmatrix}}_{K} \underbrace{\begin{bmatrix} 1 & -\alpha_{yz} & \alpha_{zy} \\ \alpha_{zy} & 1 & -\alpha_{zx} \\ -\alpha_{xy} & \alpha_{yz} & 1 \end{bmatrix}}_{T}. \tag{2-28}$$

The assumption is made that the x-axis of the sensor coincides with the x-axis of the body and that y-axis of the body is in the plane of x-y-plane of the sensor, then the lower triangular part under the diagonal of the matrix is reduced to zero [11, 36]. Then, matrix D is constructed as

$$D = \underbrace{\begin{bmatrix} k_x & 0 & 0 \\ 0 & k_y & 0 \\ 0 & 0 & k_z \end{bmatrix}}_{K} \underbrace{\begin{bmatrix} 1 & -\alpha_{yz} & \alpha_{zy} \\ 0 & 1 & -\alpha_{zx} \\ 0 & 0 & 1 \end{bmatrix}}_{T}. \tag{2-29}$$

The 9 parameters to be estimated are then the three scaling factors, three misalignment angles and three biases, given by $\theta_a = \{D, b_a\}$ When these parameters are known, the calibrated accelerometer measurements can be found by

$$y_{a,k}^{cal} = D^{-1}(y_{a,k} - b_a). \tag{2-30}$$

The calibration problem can be formulated as a ML estimation problem, as formulated by [35] is given by

$$\hat{\theta}_a = \arg\max_{\theta_a} p_{\theta_a}(y_{a,1:N}) = \arg\max_{\theta_a} \prod_{k=1}^{N} p_{\theta_a}(y_{a,k}|y_{a,1:k-1}). \tag{2-31}$$

Under the assumption that the measurement model is Gaussian, this formulation can be rewritten into a minimization problem. The negative log-likehood provides the expression of the following cost function

$$\hat{\theta}_a = \arg\min_{\theta_a} \frac{1}{2} \sum_{k=1}^{N} \left(||y_{a,k} - \hat{y}_{a,k|k-1}(\theta_a)||_{S_k^{-1}(\theta_a)} + \log \det S_k(\theta_a) \right). \tag{2-32}$$

This problem is non-linear as the innovation co-variance matrix S_k and $\hat{y}_{a,k|k-1}(\theta_a)$ have to be solved recursively in the MEKF to avoid a degenerative solution.

2-5   Orientation Estimation Solution

In the previously discussed sections of this chapter, the foundations have been introduced upon which an orientation estimation using a single IMU can be made. The accelerometer and gyroscope can be calibrated on forehand so that the error sources can be compensated for. After removal, the angular velocity provides the time update in the MEKF and the specific force provides the measurement update in the MEKF. The result after the MEKF updates is the rotation. This scheme is summarized in Figure 2-1.
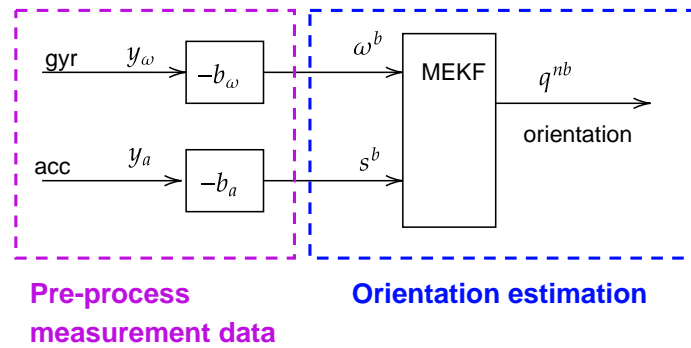
Figure 2-1: An Orientation estimation scheme using a single gyroscope and accelerometer. In the purple rectangle, the measurement data is pre-processed and in the blue rectangle, the orientation is estimated.

The orientation estimation scheme shown in Figure 2-1 forms the basis orientation estimation using an IMU. It will become apparent in Chapter 3 how Multiple IMUs can be fused to form a Synthetic IMU. This Synthetic IMU has an estimate of the angular velocity and the specific force, similar to a single IMU. The Synthetic IMU can then take the place of the single IMU for orientation estimation.

Chapter 3

Fusion of Multiple IMUs into a Synthetic IMU

This chapter expands on Chapter 2, where an orientation estimation method was introduced based on a single gyroscope and accelerometer pair. This chapter introduces how Multiple IMUs can be fused into a Synthetic IMU with more accurate estimations on the angular velocity and specific force. In Section 3-2, the identifiability conditions are shown, where it becomes apparent that it now also possible to estimate the angular acceleration. Afterwards, the Cramér-Rao Lower Bound (CRLB) is introduced and it is shown that more accurate estimates are possible than simply averaging out sensor readings in Section 3-3. In Section 3-4, a method is shown on how the measurements can be fused to estimate body kinematics. Subsequently, in Section 3-5 it is shown how the angular acceleration can aid as a motion model. Once the angular velocity and specific force are estimated, together they can classified as a Synthetic IMU. To provide good estimations on the angular velocity and angular acceleration, the position needs to be known accurately. Therefore, in Section 3-6 an accelerometer position calibration method is explained. Finally, in Section 3-7 it is shown how the information presented in this chapter can be used for orientation estimation.

3-1 Introduction

When using a single IMU for orientation estimation, it is often assumed that the accelerometer only measures the linear acceleration. This results in the measurement equation as shown in (2-27) and is restated here as

$$y_{a,k} = \underbrace{(a_k^s - R_k^{sn} g^n)}_{s_k^s} + b_{a,k}^s + e_{a,k}^s.$$

This can be a good approximation, however, if there is high rotational motion and the accelerometer is far away from the origin, the accelerometer will experience additional forces. This motivates the user to estimate the rotational motion in the accelerometer measurement.

The benefit here is twofold. Firstly, the rotational motion does not influence the estimate of the specific force. Secondly, more information on the rotational motion becomes available.

Two additional forces act on the accelerometer, the Euler force and the Centrifugal force. The specific force is the same magnitude for all accelerometers. However, the rotational acceleration increases linearly with ρ. The angular acceleration $\dot{\omega}_k$ induces the Euler force and the angular velocity ω_k induces the Centrifugal force. The effects the forces on the IMU array are shown in Figure 3-1.
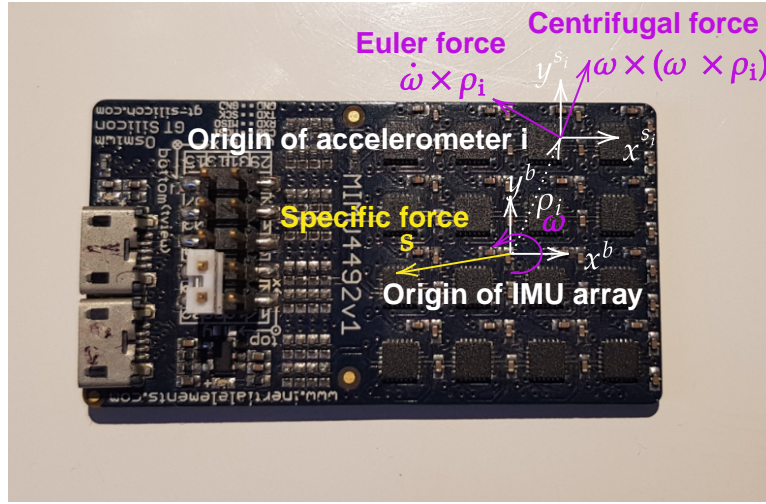
Figure 3-1: IMU array experiencing linear (yellow) and rotational (purple) motion, resulting in a specific force s, Centrifugal force $\omega \times (\omega \times \rho)$ and Euler force $\dot{\omega} \times \rho$. The angular velocity ω, angular acceleration $\dot{\omega}$ and relative position of an accelerometer ρ_i are shown. Recreated and adapted from [3].

Adding these forces to the accelerometer measurement equation gives

$$y_{a,k} = s_k^s + R^{sb}\left(\omega_k^b \times (\omega_k^b \times \rho) + \dot{\omega}_k^b \times \rho\right) + b_{a,k}^s + e_{a,k}^s, \tag{3-1}$$

where $\dot{\omega}_k^b$ denotes the angular velocity and ρ denotes the relative distance between origin of the accelerometer and the origin of the IMU array.

Measurement equation (3-1) is non-linear and has added extra terms that need to be estimated. This provides several challenges that need to be overcome as a single tri-axial accelerometer will not be able to estimate all the parameters as the problem is underdetermined. To understand how many accelerometers and gyroscopes are needed to get a unique solution the identifiability conditions for are identified, which will be shown in Section 3-2.

In literature, a distinction is made between accelerometer-only arrays and Multiple IMU arrays. The Identifiability conditions are shown for Multiple IMU arrays is largely same for accelerometer-only arrays. The main difference that separates the two is the ability to identify the sign of the angular velocity ω_k. This can be resolved by using a motion model prior for the angular velocity. The angular acceleration as a motion model will be shown in Section

3-5. Additional methods have been developed to resolve the sign ambiguity and the reader is referred to [15] for an overview.

3-2 Identifiability Conditions of the specific force, angular velocity and angular acceleration

For Multiple IMUs the identifiability conditions of the angular acceleration is dependent on the number of accelerometers [14] and their relative position ρ. The measurement models of the accelerometer and the gyroscopes are defined as [14]

$$y_{a,k} = s_k + \dot{\omega}_k \times \rho + \omega_k \times (\omega_k \times \rho) + e_{a,k}, \tag{3-2a}$$

$$y_{\omega,k} = \omega_k + e_{\omega,k}. \tag{3-2b}$$

The accelerometer measures both the specific force s and the angular acceleration $\dot{\omega}_k$ linearly. The accelerometer measures the angular velocity ω_k non-linearly, while the gyroscopes measure the angular velocity ω_k linearly. The angular velocity and angular acceleration cross products can be rewritten intro skew-symmetric matrices by introducing the cross-product matrix $[x\times]$. A real skew-symmetric matrix of size $n \times n$ has eigenvalues that are purely imaginary or zero, for a 3×3 skew-symmetric matrix this implies a rank of either 2 or 0 [38]. The skew-symmetric matrix is defined as

$$[x\times] \triangleq \begin{bmatrix} 0 & -x_3 & x_2 \\ x_3 & 0 & -x_1 \\ -x_2 & x_1 & 0 \end{bmatrix}. \tag{3-3}$$

The measurement equations can now be separated into a non-linear part $h(\omega_k)$ and a linear part H as seen below. The non-linear part holds information on the angular velocity while the linear part holds information on the angular acceleration and specific force.

In the formulation below, the relative positions of the accelerometers, denoted by ρ are time-invariant while the other variables θ_k and ω_k are time-varying and are estimated each time-step. The resulting expression is found below, (note that the timestep $*_k$ is left out for brevity)

$$\underbrace{\begin{bmatrix} y_{a_1} \\ \vdots \\ y_{a_N} \end{bmatrix}}_{Y_a} = \underbrace{\begin{bmatrix} [\omega\times]^2\rho_1 \\ \vdots \\ [\omega\times]^2\rho_N \end{bmatrix}}_{h_a(\omega)} + \underbrace{\begin{bmatrix} -[\rho_1\times] & \mathcal{I}_3 \\ \vdots & \vdots \\ -[\rho_N\times] & \mathcal{I}_3 \end{bmatrix}}_{H_a} \underbrace{\begin{bmatrix} \dot{\omega} \\ a \end{bmatrix}}_{\theta} + \underbrace{\begin{bmatrix} e_{a_1} \\ \vdots \\ e_{a_N} \end{bmatrix}}_{E_a}, \tag{3-4a}$$

$$\underbrace{\begin{bmatrix} y_{\omega_1}^T & \cdots & y_{\omega_N}^T \end{bmatrix}^T}_{Y_\omega} = \underbrace{\begin{bmatrix} \omega^T & \cdots & \omega^T \end{bmatrix}^T}_{h_\omega(\omega)} + \underbrace{\begin{bmatrix} e_{a_1}^T & \cdots & e_{a_N}^T \end{bmatrix}^T}_{E_\omega}, \tag{3-4b}$$

$$\underbrace{\begin{bmatrix} Y_a \\ Y_\omega \end{bmatrix}}_{Y} = \underbrace{\begin{bmatrix} h_a(\omega) \\ h_\omega(\omega) \end{bmatrix}}_{h(\omega)} + \underbrace{\begin{bmatrix} H_a \\ H_\omega \end{bmatrix}}_{H} \theta + \underbrace{\begin{bmatrix} E_a \\ E_\omega \end{bmatrix}}_{E}. \tag{3-4c}$$

From this formulation several important conditions can be established. The first one, is that when no gyroscopes are available, the angular velocity can only be estimated up to a sign ambiguity. Secondly, through analysis of H, it can be determined how many accelerometers are needed in order for H to have full rank. By assuming that the position of the first accelerometer is at the origin the rank of H becomes

$$
\mathrm{rank}(H) = \mathrm{rank}\left(\begin{bmatrix} 0_3 & \mathcal{I}_3 \\ -[\rho_2\times] & \mathcal{I}_3 \\ \vdots & \vdots \\ -[\rho_3\times] & \mathcal{I}_3 \\ \mathbf{0}_{3N,3} & \mathbf{0}_{3N,3} \end{bmatrix} \right) = 3 + \mathrm{rank}\left(\begin{bmatrix} -[\rho_2\times] \\ \vdots \\ -[\rho_N\times] \end{bmatrix} \right). \tag{3-5}
$$

It is evident that the rank of H is independent on the number of gyroscopes and solely depends on the location and the number of accelerometers placed. The locations of the accelerometers are in skew-symmetric form which has rank 2. Thus in order for matrix H to have full rank, a third accelerometer must be present that is not collinear with the other two placed sensors. The sufficient and necessary conditions for the identifiability conditions for the specific force, angular velocity and the angular acceleration are then

1. At least one gyroscope must be present.

2. At least three accelerometers are present whose locations are non-collinear.

Not only does the amount of sensors have influence on the identifiability conditions of the system, more accurate estimates can be found as well by using more sensors. For the gyroscopes this is rather simple as every gyroscope provides the same information (assuming they are of the same type). The co-variance of the estimation then scales linearly by $\frac{1}{N}$ by simply taking the average of the all the gyroscopes [3]. This simple solution is not the ideal method for the accelerometers, more sophisticated methods are presented in the next section.

3-3   Cramér-Rao Lower Bound of the specific force, angular velocity and the angular acceleration

The Cramér-Rao Lower Bound (CRLB) allows one to evaluate the performance of the estimator [39]. The CRLB is useful statistical tool that allows the user to identify how covariance of the measurement space translates to the covariance of the state space. More specifically, the CRLB gives the lower bound for all statistical unbiased estimators for a given parameter [40]. The CRLB is based on the Fisher Information Matrix (FIM) I. The FIM, as the name suggests tells us how much information can be obtained for state space. The inverse of the Fisher information matrices show the information obtained. That is, the eigenvalues of the co-variance matrix are larger than the eigenvalues of the CRLB

$$
\mathrm{Cov}(x) \succeq I(x)^{-1}. \tag{3-6}
$$

Fisher Information Matrix   The FIM is defined as follows [41], consider the linear measurement model with Gaussian noise $e \sim \mathcal{N}(0, \Sigma)$

$$y = Hx + e. \tag{3-7}$$

From this measurement equation the FIM is defined as

$$I(x) = E\left[\left(\frac{d\log(p(y|x))}{dx}\right)\left(\frac{d\log(p(y|x))}{dx}\right)^T\right], \tag{3-8a}$$

$$I(x) = H^T\Sigma^{-1}H. \tag{3-8b}$$

Information from multiple sensors is additive in the FIM [41]. This allows us to rewrite the stacked matrix into summation as

$$I(x) = \sum_{n=1}^{N} H_n^T\Sigma^{-1}H_n. \tag{3-9}$$

This can be applied to the measurement equation (3-4c) as well. First, the equation needs to be linearized around ω. The Jacobion for a single accelerometer and gyroscope pair of $h(\omega)$ is found to be [16]

$$J_{h,n} = \begin{bmatrix} ([[\rho_n\times]\omega\times] - [\omega\times][\rho_n\times]) \\ \mathcal{I}_3 \end{bmatrix}, \tag{3-10a}$$

$$H_n = \begin{bmatrix} -[\rho_n\times] & \mathcal{I}_3 \\ 0_3 & 0_3 \end{bmatrix}. \tag{3-10b}$$

The information matrices of the accelerometer and gyroscopes can then be found as

$$I_n = \begin{bmatrix} J_{h,n}^T \\ H_n^T \end{bmatrix} Q_n^{-1} \begin{bmatrix} J_{h,n} & H_n \end{bmatrix}, \tag{3-11}$$

where Q_n is Gaussian white measurement noise of the specified accelerometer and gyroscope pair. $N_{max} = \max(N_{acc}, N_{gyr})$, such that every $J_{h,n}$ and H_n contains information of an accelerometer or gyroscope. If the $N_{acc} < N_{gyr}$ or $N_{acc} > N_{gyr}$ then the corresponding $J_{h,n}$ and H_n would be left empty as there is no sensor information. The formulation above can again be summed as information is additive, resulting in

$$I = \sum_{n=1}^{N_{max}} I_n = \sum_{n}^{N_{max}} \begin{bmatrix} J_{h,n}^T \\ H_n^T \end{bmatrix} Q_n^{-1} \begin{bmatrix} J_{h,n} & H_n \end{bmatrix}. \tag{3-12}$$

This formulation can then be expressed in its stacked equivalent as

$$I(\theta) = \begin{bmatrix} J_h^T \\ H^T \end{bmatrix} Q^{-1} \begin{bmatrix} J_h & H \end{bmatrix}, \tag{3-13}$$

The derivation of which was done by [14] under a few assumptions. The assumptions are as follows

1. The sensors are placed in a 2D plane with the origin at the center.

2. The measurements errors are uncorrelated

3. The accelerometers have the same error variance and gyroscopes have the same error variance.

4. The sensors are placed equidistant with distance α between two neighbouring sensors.

5. The number of sensors placed is a quadratic number

By finally taking the inverse of the FIM, the CRLB for the ML estimate of the angular velocity ω, angular acceleration $\dot{\omega}$ and the specific force s can be found. The results here are based solely on the measurement equation as given in (3-4c). The results of these are shown below in equations (3-14), (3-15) and (3-16).

CRLB of the Specific force

$$I_s^{-1} = \frac{\sigma_a^2}{N_a} \mathcal{I}_3. \tag{3-14}$$

The previous equation shows that the accuracy of the information on linear acceleration obtained is inversely proportional to the number of accelerometers placed on the body. It also shows that the accuracy of the information obtained is independent on the geometry of the system.

CRLB of the Angular velocity

$$I_\omega^{-1} \overset{(|\omega| \geq \gamma)}{=} \frac{6\sigma_a^2}{\alpha_a^2(N_a^2 - N_a)} \begin{bmatrix} \frac{1}{\omega_x^2 + \omega_y^2} & 0 & * \\ 0 & \frac{1}{\omega_x^2 + \omega_y^2} & * \\ * & * & \frac{1}{2\omega_z^2} \end{bmatrix}. \tag{3-15}$$

It is of interest to know how the accelerometers estimate angular velocity, therefore, it is assumed that the gyroscopes are saturated: $|\omega| > \gamma$, where $\gamma \in \mathbb{R}$ is a positive constant and defined as the saturation threshold of the gyroscopes. Some off-diagonal entries have been left out for conciseness. It can then be seen that the information obtained about the rotational velocity is inversely proportional on the number of accelerometers placed squared N_a^2 and the distance between the accelerometers squared α_a^2. Finally, it can be observed that the information obtained is independent of the geometry of the system.

CRLB of the Angular acceleration

$$I_{\dot{\omega}}^{-1} \overset{(\omega=0)}{=} \frac{12\sigma_a^2}{\alpha_a^2(N_a^2 - N_a)} \begin{bmatrix} 1 & 0 & 0 \\ 0 & 1 & 0 \\ 0 & 0 & \frac{1}{2} \end{bmatrix}. \tag{3-16}$$

The information achieved from the previous equation is most accurate when the angular velocity is zero. Furthermore, the information obtained for the angular acceleration is proportional to the distance between the accelerometers squared α_a^2 and the number of accelerometers placed squared N_a^2.

3-4 Fusing Multiple IMUs into a Synthetic IMU using Seperable Least Squares

The previous section discusses how much information can be obtained from the angular velocity ω, angular acceleration $\dot{\omega}$ and specific force s. The problem formulation of the stacked measurements is, however, partly non-linear. One approach to solving the non-linear problem is the separable least squares method. In this method, the non-linear part is separated from the linear part. The non-linear terms can be found using Gauss-Newton optimization, resulting in a weighted least squares solution for the remaining linear part. How the estimates can be calculated is summarized in Algorithm 3, from [14]. Separable Least Squares (SLS) can be applied to a niche selection of non-linear equations, where part of the state vector enters the measurement vector [41]. This is the case for (3-4c) as is shown by [14], where the measurement equation is party linear. The non-linear part of the equation can enter the measurement vector and then WLS can be used to find the linear part. The methodology of SLS applied to (3-4c) is shown below.

First, the non-linear part can be fixed at ω^* such that a WLS expression can be found for the linear part θ. This is denoted by

$$Y = h(\omega^*) + H\theta(\omega^*) + E, \tag{3-17a}$$

$$\hat{\theta}(\omega^*) = (H^T Q^{-1} H)^{-1} H^T Q^{-1} (y - h(\omega^*)). \tag{3-17b}$$

Here, $\hat{\theta}$ is assumed to be stochastic and distributed as

$$\theta \sim \mathcal{N}(\hat{\theta}, (H^T Q^{-1} H)^{-1}), \tag{3-18}$$

and it is assumed that the stochastic error of $\hat{\theta}$ is independent in time [42]. The result of $\hat{\theta}$ can then be substituted back into Equation (3-4c), which results in

$$Y - h(\omega) = H\hat{\theta} + E. \tag{3-19}$$

The formulation above is frequently used in sensor array processing as the new covariance gives a better estimate of the covariance as it includes the structure of the array [43]. The covariance of the two stochastic sources are independent and additive, the expression can be expressed as

$$Y - h(\omega) \sim \mathcal{N}(H\hat{\theta}, H(H^T Q^{-1} H)^{-1} H^T + Q), \tag{3-20}$$

where the proof can be found in [44]. The corresponding Information matrix is given by [14] and is expressed as

$$P = Q^{-1} - Q^{-1} H (H^T Q^{-1} H)^{-1} H^T Q^{-1}. \tag{3-21}$$

The solution for $\hat{\omega}$ can then be expressed as [14]

$$\hat{\omega} = \arg\max_{\omega} (\mathcal{L}(\omega)), \tag{3-22}$$

where $\mathcal{L}(\omega)$ is defined as

$$\mathcal{L}(\omega, \hat{\theta}(\omega)) = -\frac{1}{2} ||Y - h(\omega)||_P^2 + c, \tag{3-23}$$

Algorithm 3: Fusion of the MIMU measurements to estimate ω_k and θ_k

---

Pre-process the data ;
Initialize ω_0, $k = 0$;

$$\hat{\omega}_0 = \left((\mathbf{1}_{N_\omega}^T \otimes \mathcal{I}_3)Q_\omega^{-1}(\mathbf{1}_{N_\omega} \otimes \mathcal{I}_3)\right)^{-1} (\mathbf{1}_{N_\omega}^T \otimes \mathcal{I}_3)Q_\omega^{-1}Y_\omega,$$

$$H_{s,i} = \begin{bmatrix} [-\rho_i\times] & \mathcal{I}_3 \end{bmatrix}, \qquad H_\omega = \mathbf{0}_{3N_\omega,6}, \qquad J_{\omega,h} = \mathbf{1}_{N_\omega} \otimes \mathcal{I}_3.$$

Stack ;

$$H = \begin{bmatrix} H_{s_1}^T & \dots & H_{s_{N_s}}^T & H_\omega^T \end{bmatrix}^T,$$

while *Not converged* **do**

    for $i = 1 : N_s$ **do**

$$J_{s_i,h}(\hat{\omega}_k) = ([[\rho_i\times]\hat{\omega}_k\times] - [\hat{\omega}_k\times][\rho_i\times]) ,$$
$$h_{s,i}(\hat{\omega}_k) = [\hat{\omega}_k\times]^2\rho_i.$$

    end

$$h_{\omega,i}(\hat{\omega}_k) = \mathbf{1}_{N_\omega} \otimes \hat{\omega}_k.$$

    Stack ;

$$J_h(\hat{\omega}_k) = \begin{bmatrix} J_{s_1,h}^T(\hat{\omega}_k) & \dots & J_{s_{N_s},h}^T(\hat{\omega}_k) & J_{\hat{\omega},h}^T(\hat{\omega}_k) \end{bmatrix}^T,$$
$$h(\hat{\omega}_k) = \begin{bmatrix} h_{s_1}^T(\hat{\omega}_k) & \dots & h_{s_{N_s}}^T(\hat{\omega}_k) & h_\omega^T(\hat{\omega}_k) \end{bmatrix}^T.$$

    Gauss-Newton iteration ;

$$\hat{\omega}_{k+1} = \hat{\omega}_k + \left((J_h^T(\hat{\omega}_k)PJ_h(\hat{\omega}_k))\right)^{-1} J_h^T(\hat{\omega}_k)P\left(Y - h(\hat{\omega}_k)\right).$$

    $k = k + 1$

end

$$\hat{\theta} = (H^TQ^{-1}H)^{-1}H^TQ^{-1}(Y - h(\hat{\omega}_k))$$

---

where c is a constant remainder and negligible in the minimization operation. The expression of $\hat{\omega}$ can now take the form of

$$\hat{\omega} = \arg\min_\omega ||Y - h(\omega)||_P^2 \tag{3-24}$$

This problem formulation can be solved using a Gauss-Newton algorithm. This algorithm is explained in Appendix C.

3-5   Angular Acceleration as a Motion Model

Previously, in Chapter 2, the INS for a single gyroscope and accelerometer pair was established. In this chapter, however, it has been shown that when multiple IMUs are used, they can be fused to not only obtain more accurate estimates of the angular velocity and specific force but also to estimate the angular acceleration. The angular acceleration can be used as a motion model to add additional information on the angular velocity.

The work presented in [14], which has been has been described in Section 3-4, describes a ML estimator which fuses the measurements in each individual time step. There is no relationship that couples the dynamics from one time step to the next time step. Based on their work in [14], the ML estimation of ω has been extended into a MAP estimation in [16] using motion models. The formulation presented in [16] takes a smoothing approach. This approach, however, would require all the data to be known and thus cannot be used in real time. The same motion models can also be applied as a one step ahead predictor.

The angular acceleration at time step k can now be used as a prior on the angular velocity at time step $k+1$. The motion model gives a prior of the angular velocity $\tilde{\omega}_{k+1}$ which takes the form of

$$\tilde{\omega}_{k+1} = \hat{\omega}_k + T\dot{\hat{\omega}}_k, \tag{3-25}$$

where

$$\hat{\omega}_k = \omega_k + e_{\omega,k}, \tag{3-26a}$$

$$\dot{\hat{\omega}}_k = \dot{\omega}_k + e_{\dot{\omega},k}, \tag{3-26b}$$

where $e_{\omega,k} \sim \mathcal{N}(0, \Sigma_\omega)$ and $e_{\dot{\omega},k} \sim \mathcal{N}(0, \Sigma_{\dot{\omega}})$ are Gaussian white noise. These two error sources can be assumed to be independent [16], this leads to the summation of their error giving the motion model as

$$\tilde{\omega}_{k+1} = \omega_k + \dot{\omega}_k + e_{\tilde{\omega},k}, \tag{3-27}$$

where $e_{\tilde{\omega},k} \sim \mathcal{N}(0, \Sigma_{\tilde{\omega}})$. In the current form, no motion models (random walk) models are used for the specific force and the angular acceleration, however, they can be Incorporated in the same manner. Only motion model (3-27) such that the potential benefits of this motion model can be highlighted. Additionally to the increase in accuracy, [16] also has shown that the motion model allows identifiability conditions described in Section 3-2 to be altered to be free of any gyroscope. The sign ambiguity now disappears as prior information is available. This allows the method described in Section 3-4 for the extension towards gyro-free arrays.

3-6   Position Calibration of Accelerometers

The fusion method described in 3-4 does not assume any error in the relative locations. Therefore, the relative spatial geometry between accelerometers must be known accurately for the optimal fusion of the measurements [14]. A geometric calibration for the relative positions, based on their work in [14], is shown in [13]. The calibration allows the user to estimate the relative positions with enough precision to make the estimation in Section 3-4 reliable [13].

The calibration algorithm is summarized below by making use of the measurement models as in (3-2a) and its stacked form (3-4c)

As initial position, the relative distances can be measured with e.g. a ruler and the first accelerometer is set at the origin. Afterwards, set an arbitrary accelerometer as the reference position ρ_1. The other positions are updated relative to this reference position. Furthermore, one can define the state x_k as

$$x_k = \begin{bmatrix} \omega_k^T & \dot{\omega}_k^T & T_k \end{bmatrix}^T \tag{3-28}$$

for the unknown motion dynamics at every time step, this allows one to define the ML estimation problem as

$$\{\hat{x}_{1:K}, \hat{\rho}_{1:N}\} = \arg \max_{x_{1:K}, \rho_{1:N}} p(Y_{1:K}|x_{1:K}, \rho_{1:N}). \tag{3-29}$$

Assuming the motion dynamics to be independent in time the problem can be reformulated into

$$\{\hat{x}_{1:K}, \hat{\rho}_{1:N}\} = \arg \max_{\theta_\rho} \prod_{k=1}^{K} \max_{x_k} p(y_k|x_k, \rho_{1:N}), \tag{3-30}$$

such that x_k is found to maximize the probability of observing measurement y_k and θ_ρ to maximize the probability of observing all measurements $y_{1:K}$. A solution to this problem can be found by alternatively calculating and fixing $x_{1:k}$ and θ_ρ until a stopping criteria is satisfied. To find the solution to $x_{1:k}$ the solution from Section 3-4 can be used. Additionally the solution for θ_ρ can be found as follows

$$\rho_i = \left(\sum_{k=1}^{K} \Omega_k^T \Omega_k \right)^{-1} \left(\sum_{k=1}^{K} \Omega_k^T (y_{a_i,k} - s_k^b) \right). \tag{3-31}$$

Combining these two proposed solutions, Algorithm 4, from [13], can be implemented

---

Algorithm 4: Position calibration for a sensor array

Set reference position ρ_1 ;
Set initial estimate for $\hat{\rho}_{2:N_a}$, set $j = 1$;
while *Not converged* **do**

    for $k = 1 : N$ **do**

        ML estimate for $\hat{x}_k$ can be found using Algorithm 3.

$$\hat{x}_k = \arg\max_x p(Y_k | x_k, \hat{\rho}_{1:N_a}),$$

$$\Omega_k = [\hat{\omega}_k \times]^2 + [\dot{\hat{\omega}}_k \times].$$

    end

$$C = \left(\sum_{k=1}^{N} \Omega_k^T \Omega_k \right)^{-1}$$

    for $i = 2 : N_a$ **do**

$$\hat{\rho}_i = C * \left(\sum_{k=1}^{N} \Omega_k^T \left(y_{a_i,k} - \hat{s}_k \right) \right).$$

    end

    $j = j + 1$

end

3-7   Multiple IMUs Inertial Navigation Solution

An orientation estimation has been shown previously in Section 2-5, where use was made of a single gyroscope and accelerometer pair. In this chapter the pose estimation is done in the same manner and data is pre-process in the same manner. This Chapter introduced how multiple sensors can be fused together into a Synthetic IMU, where the synthetic IMU is classified as the final estimates of the angular velocity and the specific force. Furthermore, it also allows for the estimation of the angular acceleration, which in turn can be used as a motion model prior to further improve the estimation of the angular velocity. An updated orientation estimation scheme is shown in Figure 3-2 where the additional benefit the fusion of IMUs and the motion model are enclosed by the red rectangle.
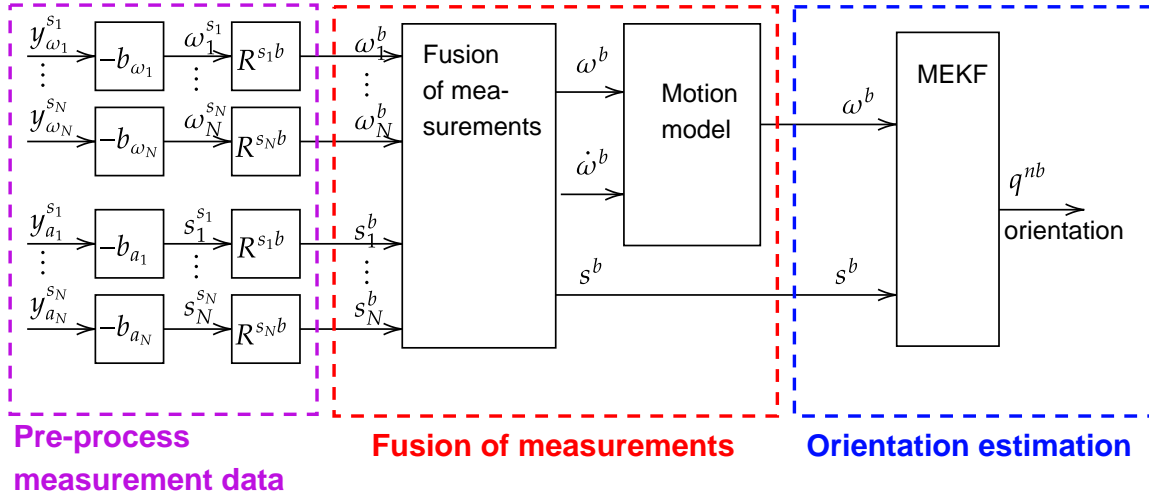
Figure 3-2: An orientation estimation scheme using Multiple IMUs. In the purple rectangle, the measurement data is pre-processed after which in the red rectangle all the measurement are fused into a single Synthetic IMU. The synthetic IMU can then estimate the orientation as seen in the blue rectangle

The theory presented in this chapter largely follows the works of [14], [16] and [13]. This chapter serves as a basis for the simulation setup in Chapter 4 and will be used to present a novel parity space method for FDI as will be shown in Chapter 5.

Multiple IMUs Simulation setup and results

This chapter introduces how the simulations will be performed, in Section 4-3 a general procedure on how to generate measurement data is explained. This will be used as a basis for measurement data generation in the simulations. In Chapter 3 it was introduced how multiple IMUs can be fused to form a Synthetic IMU. It was also shown that additional information became available in the form of angular acceleration which was used as a motion model. The relationship between certain parameters and how much information can be obtained was also introduced. How these relationships will be verified using Monte Carlo simulation using several parameters is shown in Section 4-2. Afterwards, the results are shown and discussed in Section 4-4. An additional simulation setup and results are shown in Sections 4-5 and 4-6 respectively. Where different setups are tested on how accurate the angular velocity and specific force estimate is against an higher-grade IMU. _____ herschrijven

4-1 Introduction

In Chapter 3 it was shown how Multiple IMUs can be fused. After fusion we had an estimated covariance of the specific force s, angular velocity ω, but also of the angular acceleration $\dot{\omega}$. How these covariances change according to different parameters was also shown. These are briefly summarized (with the assumption that $\omega = \omega_x = \omega_y = \omega_z$ for brevity) here as:

$$\underbrace{I_\omega^{-1} \overset{(|\omega| > \gamma)}{\propto} \frac{\sigma_a^2}{\alpha_a^2(N_a^2 - N_a)\omega^2}}_{\text{Angular velocity}}, \qquad \underbrace{I_{\dot{\omega}}^{-1} \overset{(\omega=0)}{\propto} \frac{\sigma_a^2}{\alpha_a^2(N_a^2 - N_a)}}_{\text{Angular acceleration}}, \qquad \underbrace{I_s^{-1} \propto \frac{\sigma_a^2}{N_a}}_{\text{Specific force}}, \qquad (4\text{-}1)$$

where I denotes the FIM, σ_a denotes the variance of the accelerometer, γ denotes the saturation value for the gyroscopes, N_a denotes the number of accelerometers and α denotes the distance between two adjacent sensors. These analytical relationships were found by [14] for an array configuration, where several assumptions were made. These assumptions are restated here:

1. The sensors are placed in a 2D plane with the origin at the center.

2. The measurement errors are uncorrelated

3. The accelerometers have the same error variance and gyroscopes have the same error variance.

4. The sensors are placed equidistant with distance α between two neighbouring sensors.

5. The number of sensors placed is a quadratic number

One of the limitations is the assumption that the sensors are placed in a 2D plane. Another limitation of the assumptions is that the sensors are placed equidistantly. These assumptions are violated for the MIMU4844 IMU array from Inertial Elements shown in Figure 1-3. A schematic representation of this IMU array is shown in Figure 4-1. In the IMU array, two layers of sensors are placed on top of each other. This makes the IMU array more compact and easier to use. However, as some assumptions are violated, the question is: does this have an influence on the covariance of the specific force, angular velocity and the angular acceleration? This will be shown in the results in Section 4-4.

It was also shown in Chapter 3 that an additional motion parameter can be estimated, the angular acceleration. The angular acceleration can be used as a motion model prior for the angular velocity, as shown in [16]. They also noted in their work that the angular acceleration and specific force can be modeled as a random walk model as well. In this chapter, different motion models are used in a simulation to compare a Synthetic IMU against a higher-grade IMU.

There are two configurations for a Synthetic IMU that will be tested against a higher-grade IMU. The first is the MIMU4844 IMU array, as shown in Figure 1-3. The distance between the sensors is very small for this configuration $\approx 5mm$. If the same sensors were instead scattered across the surface of a human arm (resulting in a distance of $\approx 100mm$ between sensors in the x-axis). This would result in more accurate estimations of the angular velocity. The second configuration represents a human arm and will be shown in Figure 4-6. The IMUs are placed equidistantly on the surface of a cylinder of length $0.3m$ and radius $0.05m$. The results will be shown in Section 4-6.

4-2   Simulation setup to estimate the CRLB of the MIMU4844 array

The simulation is based on the MIMU4844 IMU array, with 32 accelerometers and 32 gyroscopes from Inertial Elements. This is done to analyze the limitations of the assumptions made in [14] with the MIMU4844 IMU array.

Violation of previous assumptions   The assumptions made in [14] that do not hold for the MIMU4844 IMU array are:

- The sensors are placed in a 2D plane with the origin at the center.

- The accelerometers have the same error variance and gyroscopes have the same error variance.

- The sensors are placed equidistant with distance α between two neighbouring sensors.

- The number of sensors placed is a quadratic number.

While the first and the last assumption can be met by only using one of the two layers as shown in Figure 1-3, in reality, one would want to use all the sensors, not part of the sensors.

Assumptions of this simulation   For simulation purposes, the estimated positions for the accelerometers and estimated covariances for the gyroscopes and accelerometers were used.

- Accelerometer covariances are as in Figure D-4 and roughly equal to $0.04\mathcal{I}_3$ m/s^2,

- Gyroscope covariances are as in Figure D-3 and roughly equal to $0.01\mathcal{I}_3$ rad/s,

- The positions of the IMUs with their respective numbers are shown in Figure 4-1.

- The biases and cross-axis inference can be compensated for properly and are, therefore, left out.

- The rotational velocity (unless varied) will be set at $\omega = \begin{bmatrix} 1 & 1 & 1 \end{bmatrix}^T$ rad/s.

For the chosen angular velocity magnitude, this can be considered a fast movement for the arm as after 1 second the arm has rotated almost 60° around each axis.

Calibration   The IMU array has 32 gyroscopes and 32 accelerometers each not yet calibrated. First, the gyroscopes are calibrated for the covariances and biases as discussed in Section 2-4-1. Afterwards, the accelerometers can be calibrated for as discussed in Section 2-4-2 for its bias, covariance and cross-axis interference. After all sensors have been calibrated, the calibration for the relative positions can be done as discussed in Section 3-6. The positions and coordinate frames of the IMUs are plotted in Figure 4-1. For the simulation, it is assumed that the calibrated positions are the true positions.

Configuration   The real-life array, shown in Figure 1-3, consists of two layers of sensors on top of each other. In each layer, the axes of the sensors point in the same direction. However, the axes of the two layers do not. The locations, orientations of each sensor after calibration is illustrated in Figure 4-1.
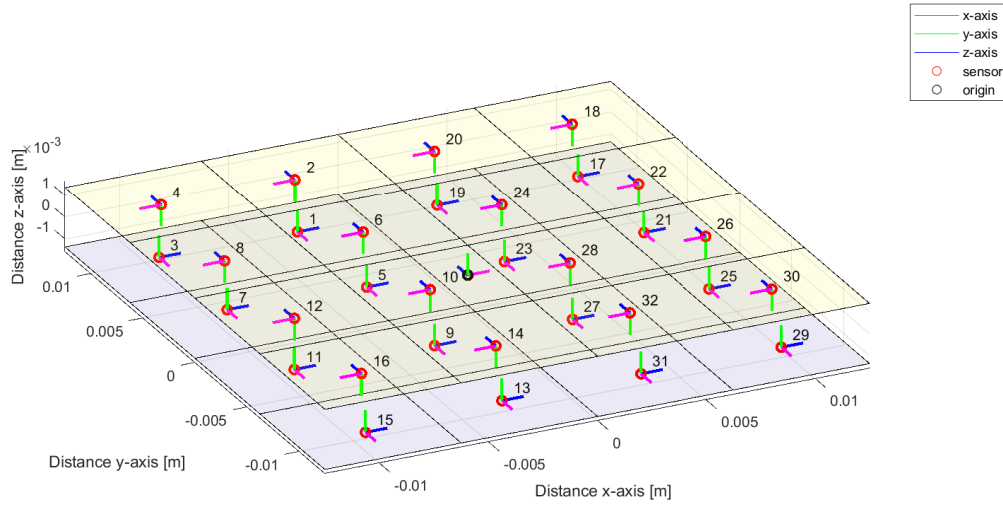
Figure 4-1: Locations and orientation of 32 accelerometers and gyroscopes of the MIMU4844 IMU array from Inertial Elements. The IMUS are located with a certain error on two layers on top of each other. The IMUs in each layer have their axes pointing in the same direction.

Each IMU had a slight offset in the orientation and a misalignment error. It is assumed that it is known a priori how the IMUs are rotated and what the misalignment error is. More specifically, the rotation matrices $R^{s_i b}$ and $R^{s_j b}$ for $i = 1 : N_a$ and $j = 1 : N_\omega$ are known a priori with sufficient accuracy and are, therefore, neglected in the simulation.

Varying parameters   Several different varying parameters were used for the simulation. From four parameters, the results of four are shown in Section 4-4. These are

- Varying number of accelerometers,

- Varying relative distance between sensors,

- Varying displacement of the origin.

- Varying magnitude of the angular velocity.

An additional different variables was compared as well. This results is shown in Appendix E,

- Varying number of gyroscopes.

For all simulations, a Monte Carlo simulation was run with 10^3 realizations to approximate the ML CRLB. The results of the Monte Carlo simulation are also shown in every plot.

4-3   Generating Simulation Measurement Data for Multiple IMUs

As is previously shown, the measurement equation of the gyroscope depends on the angular velocity and Gaussian white noise. The accelerometer, in turn depends on the angular velocity, the angular acceleration, the specific force and also Gaussian white noise. The measurement equations (3-2a) are repeated here for clarity

$$y_{a,k} = s_k + \dot{\omega}_k \times \rho + \omega_k \times (\omega_k \times \rho) + e_{a,k},$$
$$y_{\omega,k} = \omega_k + e_{\omega,k}.$$

The angular velocity and angular acceleration is the same for every accelerometer, and has to be calculated only once. By introducing the term Ω_k as

$$\Omega_k^b = [\dot{\omega}_k^b \times] + [\omega_k^b \times]^2, \tag{4-3}$$

where $i = 1 : N_a$ accelerometers $j = 1 : N_\omega$ gyroscopes. .The measurement equations of the accelerometers and gyroscopes can be expressed as

$$y_{a_i,k} = R^{s_i b} \left(\left(a_k^b - R_k^{bn} g^n \right) + \Omega_k^b \rho_i \right) + b_{s_i k}^{s_i} + e_{a_i,k}^{s_i}, \tag{4-4a}$$

$$y_{\omega_j,k} = R^{s_j b} \omega_k^b + b_{\omega_j}^{s_j} + e_{\omega_j,k}^{s_j}. \tag{4-4b}$$

The sensors can be placed at any location but also in any orientation. The sensor frames and body frame do not necessarily align. For the gyroscope measurement equation, the angular velocity is expressed in the body frame and is measured in the sensor frame. Afterwards, Gaussian white noise and a bias can be added. For the accelerometers, the angular motion can be grouped together into a single term Ω_k^b. The linear motion is the combination of the linear acceleration and the gravity vector. The linear acceleration can be set in the body frame, however, the gravity vector is constant in the navigation frame and must be rotated towards the body frame using rotation matrix R_k^{bn}.

The rotation matrix can be found from the quaternion q^{nb}, which keeps track of the rotation from body to navigation frame as

$$R_k^{bn} = \left[q_v q_v^T + q_0^2 \mathcal{I}_3 + 2q_0 [q_v \times] + [q_v \times]^2. \right] \tag{4-5}$$

The quaternion can be updated (note that the quaternion after the update will be at unit length) for every time step as

$$q_k^{nb} = \exp_q(\frac{\omega_k^b}{2}) \odot q_{k-1}^{nb}. \tag{4-6}$$

The linear acceleration and the rotational velocity in the body frame can now be set as desired. The angular acceleration can be found by taking the discrete time derivative of the angular velocity as

$$\dot{\omega}_k^b = \frac{\omega_{k+1}^b - \omega_k^b}{T}. \tag{4-7}$$

The assumptions are made that the bias is constant and that noise is additive. It is further assumed that the relative accelerometer locations $\rho_{1:N_a}$, biases and all rotation matrices $R^{s_i b}$ and $R^{\omega_j b}$ are known a priori. The generation of simulation data is summarized in Algorithm 6 in Appendix E.

4-4   Results on the covariance of the specific force, angular velocity and angular acceleration of the MIMU4844 array

In this section the results are shown of the covariance of the angular velocity, the angular acceleration and the specific force for a varying number of accelerometers, a varying relative distance between sensors and a varying displacement of the origin.

4-4-1   Varying number of accelerometers

The plots for the number of accelerometers below are shown from 3 to 32 accelerometers as that is the minimum amount of accelerometers necessary to comply to the identifiability conditions as discussed in 3-2. There were 32 gyroscopes used and the angular velocity was set to $\omega = \begin{bmatrix} 1 & 1 & 1 \end{bmatrix}^T$ rad/s. The results are plotted in Figure 4-2. The relationship in (4-1) is repeated for the number of accelerometers as

$$\underbrace{I_\omega^{-1} \propto \frac{1}{N_a^2}}_{\text{Angular velocity}} \quad , \qquad \underbrace{I_{\dot\omega}^{-1} \propto \frac{1}{N_a^2}}_{\text{Angular acceleration}} \quad , \qquad \underbrace{I_s^{-1} \propto \frac{1}{N_a}}_{\text{Specific force}} . \tag{4-8}$$

Angular velocity   The trace of the covariance of the angular velocity is plotted on the left of Figure 4-2. The analytical expression (blue) is verified with a MC approximation (yellow). They are both compared to trace of the covariance of the mean of all the gyroscopes (purple). From the relationship shown in (4-8), the covariance trace of the angular velocity is expected to decrease quadratically. The trace of the covariance in Figure 4-2 does not follow this expectation. Instead, the covariance remains almost constant and decreases slightly when more sensors are placed. This can be explained by that the information provided by the gyroscopes outweighs the information provided by the accelerometers. As more accelerometers are added, add a small amount of information. This shows that at this angular velocity and this configuration the mean of the gyroscopes provides roughly the same accuracy on the estimate of the angular velocity.

Angular acceleration   In the middle of Figure 4-1, the trace of the angular acceleration covariance (blue) is plotted and verified with a MC approximation (yellow). As can be seen in (4-8), the angular angular acceleration covariance is expected scale proportionally with N_a^2. However, the simulation shows that the angular acceleration scales with N_a rather than N_a^2. This can be attributed to the configuration of the array. The sensors are placed equidistantly in the xy-plane, but they are placed in two planes with small separation in the z-direction. The assumption that the relative distance is the same between sensors does not hold for this IMU array. If the angular acceleration were to be used as a motion model prior, it would contain less information.

Specific force   As shown in the right of Figure 4-2, the trace of the covariance of the specific force is plotted. The analytical covariance (blue) is verified with a MC approximation (yellow) and compared to averaging out the accelerometer measurements. By looking at (4-8), we

would expect the analytical covariance to coincide with averaged covariance. It can be seen
that the three lines overlap and thus (4-8) shows a correct relationship. A small difference
between the analytical and the averaged covariance can be observed at 3 accelerometers. This
can be explained by the displacement of the origin. As only 3 accelerometers are placed, the
origin is not in the same place as the centre of these 3 accelerometers. This effect will be
elaborated on in more detail in Section 4-4-3.

Figure 4-2: Angular velocity covariance (left) Angular acceleration covariance (mid) and Specific
force covariance (right) plotted against number of accelerometers N_a. All 32 gyroscopes were
used and the angular velocity was set at $\omega = \begin{bmatrix} 1 & 1 & 1 \end{bmatrix}^T$ rad/s and the IMU locations are based
on the MIMU4844 array also shown in Figure 4-1.

4-4-2 Varying relative distance between sensors

In this simulation, 32 accelerometers and 32 gyroscopes were used at $\omega = \begin{bmatrix} 1 & 1 & 1 \end{bmatrix}^T$ rad/s.
The relative distance was increased with a scale factor from 1 to 10^3 times ρ. This was done
to preserve the structure of the array and only the relative distance between the sensors is
increased. The results are plotted in Figure 4-3. The relationship in (4-1) is repeated for the
distance between sensors as

$$\underbrace{I_\omega^{-1} \propto \frac{1}{\alpha_a^2}}_{\text{Angular velocity}} \, , \qquad \underbrace{I_{\dot\omega}^{-1} \propto \frac{1}{\alpha_a^2}}_{\text{Angular acceleration}} \quad . \tag{4-9}$$

Angular velocity   In Figure 4-3, the analytical covariance trace (blue) of the angular velocity
is plotted and verified with a MC approximation (yellow). As a baseline, the averaged covari-
ance of the gyroscopes (purple) is also plotted. From (4-9) we would expect that the angular
velocity decreases quadratically as the scale factor increases. Initially, the analytical covari-
ance is almost the same as the averaged covariance. This is because, at this magnitude of the
scale factor, the information provided by the gyroscopes outweighs the information provided
by the accelerometers. As the magnitude of the scale factor increases, the accelerometers can
add more information to the angular velocity estimate. Eventually, at higher scale factors, the
covariance decreases quadratically. At lower angular velocities, the gyroscopes are dominant
in providing information.

Angular acceleration The analytical covariance trace (blue) of the angular acceleration and a MC approximation (yellow) are plotted in the middle of Figure 4-3. By looking at (4-9) we expect that the covariance decreases quadratically with the scale factor. The plotted results show the same trend. at higher magnitudes As was stated in the results of the angular velocity, it also decreases quadratically with the scale factor. This affects the information that the angular acceleration as a motion model prior can have. More specifically, increasing the distance between the accelerometers does increase the information gained from the angular acceleration as a motion model prior.

Specific force On the right in Figure 4-3 the trace of the analytical covariance trace of the specific force covariance (blue) is plotted with a MC approximation (yellow). Additionally, the averaged covariance trace of all accelerometers is plotted (purple) as a baseline. The expectation from (4-9) is that the specific force remains the same as the baseline. The results coincide with the expectation from (4-9).
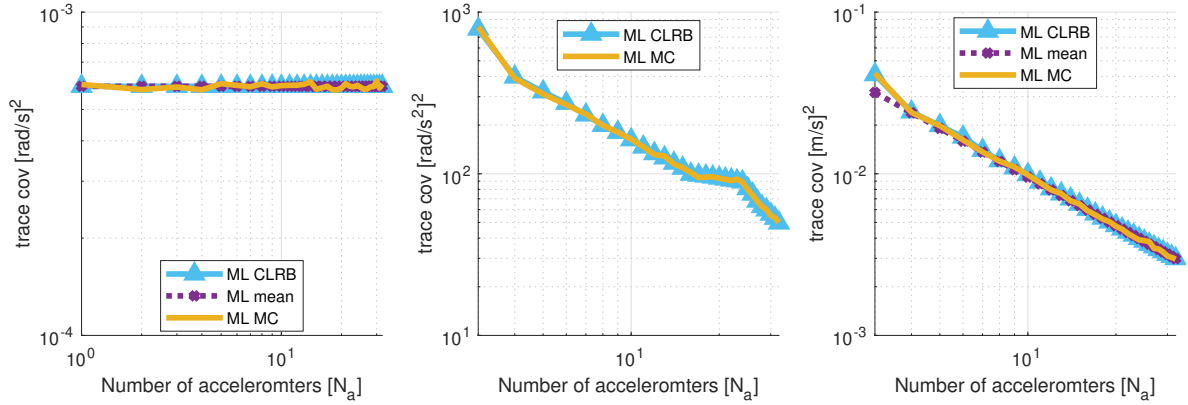

Figure 4-3: Angular velocity covariance (left) Angular acceleration covariance (mid) and Specific force covariance (right) plotted against distance between sensors. The base MIMU4844 array locations with 32 accelerometers and 32 gyroscopes is as in Figure 4-1. The array is scaled up with a scale factor from 1 to 10^3 the original configuration size. The angular velocity was set at $\omega = \begin{bmatrix} 1 & 1 & 1 \end{bmatrix}^T$ rad/s.

4-4-3 Varying displacement of the origin

This simulation again has 32 accelerometers, 32 gyroscopes, an angular velocity of $\omega = \begin{bmatrix} 1 & 1 & 1 \end{bmatrix}^T$ rad/s and the array structure. In this case, however, the origin was displaced, i.e. where Synthetic IMU measurements are estimated. The results are shown in Figure 4-4. The relationship in (4-1) does no include the varying displacement. We would expect that changing this origin will not affect the covariance of the specific force, angular velocity or angular acceleration.

Angular velocity The trace of the angular velocity covariance is plotted in Figure 4-4. The analytical covariance (purple) is verified numerically with a MC approximation (yellow). A baseline is added from the averaged covariance (purple) of the gyroscopes. The covariance did not change when displacing the origin of the Synthetic IMU as was expected.

Angular acceleration   In Figure 4-4 the trace of the angular acceleration is plotted in the middle. Both the analytical covariance (blue) and a MC approximation (yellow) are shown. As expected, the covariance of the angular acceleration remains constant under changing the location of the Synthetic IMU.

Specific force   On the right of Figure 4-4, the specific force covariance trace is shown. The analytical covariance (blue) is verified with a MC approximation (yellow) and compared to a baseline. The baseline is the averaged covariance (purple) of the accelerometers. We expected the covariance to remain unchanged under shifting the origin of the Synthetic IMU. As can be observed, however, the covariance starts to grow quadratically with the displacement of the origin. This does not seem problematic at first glance as the origin of the Synthetic IMU can be chosen arbitrarily, so the best choice would be in the centre. However, if these locations were to change, or sensors would be momentarily removed (as will be the case in Chapter 6). The uncertainty increase may result in a performance loss of orientation estimation. This effect was observed in future results (see Figure 6-9) and are discussed in Section **??**.

Figure 4-4: Angular velocity covariance (left) Angular acceleration covariance (mid) and Specific force covariance (right) plotted the displacement of the origin. The base angular velocity was set at $\omega = \begin{bmatrix} 1 & 1 & 1 \end{bmatrix}^T$ rad/s. The IMU locations are based on the MIMU4844 array also shown in Figure 4-1 with 32 accelerometers and 32 gyroscopes.

4-4-4   Varying magnitude of the angular velocity

For the final simulation, 32 accelerometers and 32 gyroscopes were used with the standard array configuration. The angular velocity was changed from $\omega = \begin{bmatrix} 1 & 1 & 1 \end{bmatrix}^T$ rad/s to $\omega = 10^4 \begin{bmatrix} 1 & 1 & 1 \end{bmatrix}^T$ rad/s. The results are shown in Figure 4-5. The relationship in (4-1) is repeated for the distance between sensors as

$$\underbrace{I_\omega^{-1} \propto \frac{1}{\omega^2}}_{\text{Angular velocity}} \quad . \tag{4-10}$$

Angular velocity   In the left of Figure 4-5, the trace of the covariance is plotted. The analytical covariance (blue) is verified with a MC approximation (yellow) and compared to the averaged gyroscope covariance (purple) as a baseline. At low angular velocities and using the base configuration of the MIMU4844 array, the analytical covariance is slightly below the baseline. However, as the magnitude of the angular velocity increases (from 10^2 rad/s and higher), the covariance of the angular velocity decreases quadratically. This result is in expectation with (4-10). At these higher angular velocities, the accelerometers provide more information than the gyroscopes. This verifies the use of accelerometer-only arrays in highly dynamic environments. Note that the gyroscope still provides useful information. Adding at least one gyroscope in an accelerometer-only array helps resolve the sign ambiguity.

Angular acceleration   The covariance trace of the angular acceleration is plotted in the middle of Figure 4-5. The analytical covariance (blue) is plotted and verified with a MC approximation (yellow). In (4-10) we expected that the angular acceleration covariance would remain constant, however, the assumption was made that the angular velocity was zero. At higher angular velocities, the covariance of the angular acceleration increases slightly, the impact is rather insignificant. More importantly, the angular velocity covariance decreases quadratically while the angular acceleration covariance slightly increases. This impacts the angular acceleration as a motion model prior for the angular velocity. At lower angular velocities, the angular acceleration motion model is more potent than at higher angular velocities.

Specific force   In Figure 4-5 the trace of the covariance of the specific force is shown on the right. The analytical covariance (blue) is verified with a MC approximation (yellow) and compared to the averaged covariance (purple) of the accelerometers. We expect that the specific force covariance remains invariant under changing the angular velocity and this is verified in the result.

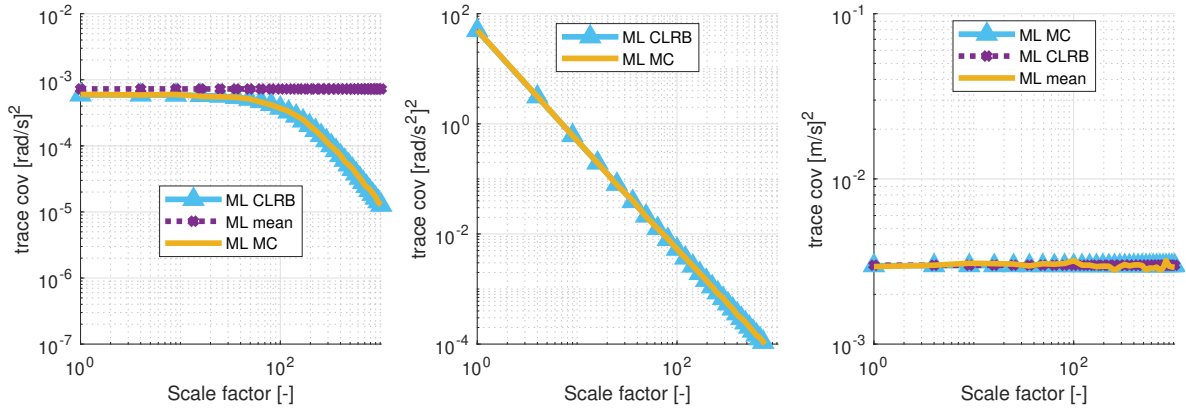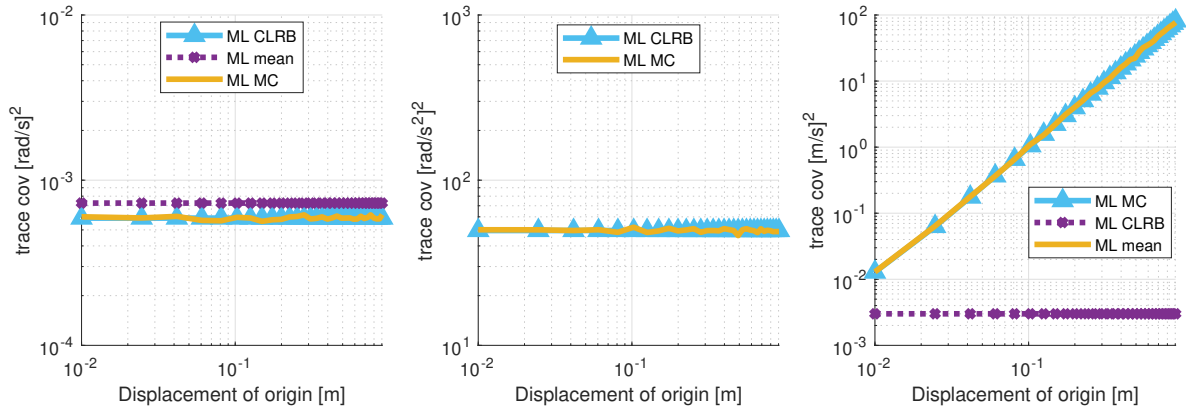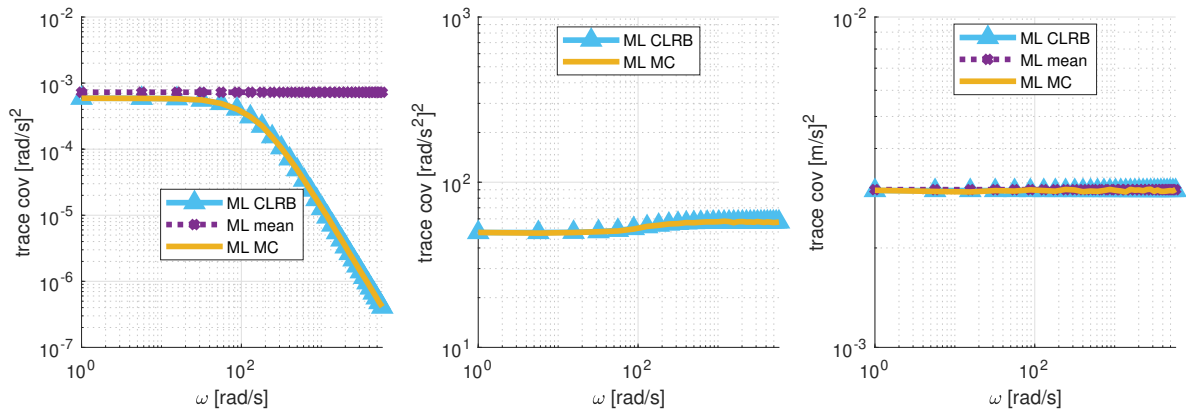**Figure 4-5:** Angular velocity covariance (left) Angular acceleration covariance (mid) and Specific force covariance (right) plotted against angular velocity ω. The base angular velocity was set at $\omega = 10^0 \begin{bmatrix} 1 & 1 & 1 \end{bmatrix}^T$ rad/s and increased to $\omega = 10^4 \begin{bmatrix} 1 & 1 & 1 \end{bmatrix}^T$ rad/s . The IMU locations are based on MIMU4844 array also shown in Figure 4-1 with 32 accelerometers and 32 gyroscopes.

4-5 Simulation setup to compare different setups against a high-grade IMU

One of the questions that is useful to analyze is how do Multiple lower-grade IMUs stand against a higher-grade IMU. To provide an answer to this question, first it must be addressed that there are many different factors that influence the answer. For this reason some assumptions have to be made. The choices and assumption made are shown below. Note that measurement data was simulated as described in Algorithm 6.

Different accelerometer configurations The first configuration that will be analyzed is the MIMU4844 IMU array from Inertial Elements. On this configuration all 32 IMUs will be used with their locations taken from their position calibration, see Figure 4-1 a reference. Another configuration to be analyzed is a cylinder the size of a human arm segment where the same IMUs are used. The radius of the cylinder is $0.05m$ and the length of the cylinder is $0.3m$, to resemble the size of a human arm. The accelerometers placed in four rings with 8 sensors. The rings are placed equidistantly in the x-axis, so that the entire length of the cylinder is used. The locations of the accelerometers can be seen in Figure 4-6.
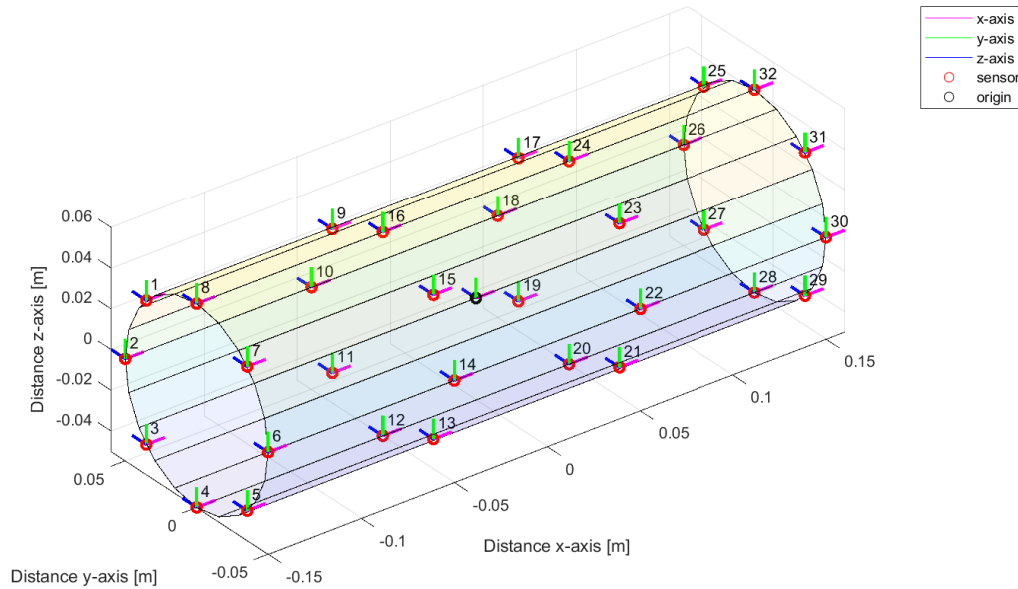
Figure 4-6: Locations and orientation of 32 accelerometers and gyroscopes pseudo-randomly placed. The IMUs are placed on the surface of the cylinder and have their sensitive axes point in different directions.

Different Angular velocity Magnitudes As was shown in the results in Section 4-4-4, the covariance of the angular velocity depends on on the magnitude of the angular velocity, that is, the angular velocity covariance decreases as the angular velocity magnitude increases.

The least amount of information that can be obtained from the accelerometers on the angular velocity is when the angular velocity is zero. The angular velocity will be set from $10^0 \begin{bmatrix} 1 & 1 & 1 \end{bmatrix}^T$ rad/s to $10^4 \begin{bmatrix} 1 & 1 & 1 \end{bmatrix}^T$ rad/s.

Different choices in motion models There are different choices to make when it comes to using motion models as a prior or not. These already have been discussed in Sections 2-2 and 3-5. In this simulation two models are assumed for the specific force and the angular acceleration; no motion model and a random walk model. The angular velocity can take no motion model, a random walk model or make use of the angular acceleration. In summary, these take the form of

$$s_{k+1} = s_k + e_{s,k}, \tag{4-11a}$$

$$\omega_{k+1} = \omega_k + e_{\omega,k}, \tag{4-11b}$$

$$\omega_{k+1} = \omega_k + \dot{\omega}_k + e_{\dot{\omega},k}, \tag{4-11c}$$

$$\dot{\omega}_{k+1} = \dot{\omega}_k + e_{\dot{\omega},k}. \tag{4-11d}$$

Constants throughout the simulation The covariance matrices of the accelerometers and gyroscopes are all set equal to $\mathcal{I}_3 0.04 \mathrm{m/s}^2$ and $\mathcal{I}_3 0.01 \mathrm{rad/s}$ respectively. The sampling rate is set at 100 Hz. No biases or misalignment errors were added as the assumption is made these can be compensated for. It is also assumed that the position of the accelerometers can be calibrated properly and hence is known with high enough accuracy. The motion model covariances were chosen to be equal to the estimated covariances. In reality, the motion model covarainces are often used as tuning parameters and are likely taken to be higher. However, for this simulation we assume that we know them with sufficient accuracy.

Higher-grade IMU As comparison, the MTi 300-series from Xsens [1] was chosen as a higher-grade IMU. The noise covariance for the gyroscope and accelerometer were found experimentally at 100 Hz as

$$\Sigma_{\omega_{\mathrm{X}}} = \begin{bmatrix} 2.096 & 0 & 00 \\ 0 & 2.076 & 0 \\ 0 & 0 & 1.474 \end{bmatrix} 10^{-6}, \qquad \Sigma_{a_{\mathrm{X}}} = \begin{bmatrix} 3.335 & 0 & 00 \\ 0 & 3.323 & 0 \\ 0 & 0 & 2.470 \end{bmatrix} 10^{-5}. \tag{4-12}$$

The higher-grade IMU was simulated without motion model for both the gyroscope and the accelerometer. Note that in reality, a motion model for the angular velocity and specific force can be chosen for the higher-grade IMU. This would further increase the accuracy of the higher-grade IMU.

4-6 Results on comparing different setups against a higher-grade IMU

4-6-1 IMU array configuration

In this configuration, where use was made of 32 gyroscopes and accelerometers, the angular velocity RMSE at lower angular velocities does not outperform the high-grade IMU from

Xsens. As the process noise covariances were taken to be equal to the estimates, it is interesting to note that the random walk model on the angular velocity performs the best. If the angular velocity gets higher than a threshold, roughly $\omega \approx 2000 \begin{bmatrix} 1 & 1 & 1 \end{bmatrix}^T$ rad/s, the IMU array, with and without motion models start to outperform the Xsense gyroscope sensor. The RMSE for the angular velocities are shown in Figure 4-7. The ratio with respect to the high-grade IMU can be seen in Table 4-1.

Figure 4-7: Synthetic IMU angular velocity covariance after fusion of the MIMU4844 IMU array of Inertial Elements. The covariances of the x-axis (left) y-axis (mid) and z-axis (right) using different motion models are shown, which are compared to MTi 300 IMU from Xsens.

There were 32 accelerometers used, which is the only influence on the specific force RMSE. the ratio of the RMSE with respect to the high-grade IMU can be seen in Table 4-1.

motion model	Angular velocity in x- y- and z- axis [rad/s]				
Angular velocity	$\omega = 10^0$	$\omega = 10^1$	$\omega = 10^2$	$\omega = 10^3$	$\omega = 10^4$
ω no motion model	14.6	14.5	11.3	1.94	0.200
ω random walk	11.4	11.4	8.95	1.52	0.157
$\dot{\omega}$ motion model	13.8	13.7	11.0	1.93	0.200
$\dot{\omega}$ random walk	13.4	13.4	10.8	1.93	0.200
Specific force					
s no motion model	7.11				
s random walk	5.59				

Table 4-1: Performance comparison different motion models of the MIMU4844 IMU array of Inertial Elements. The performance is indicated by the ratio of the RMSE with respect to the MTi 300 IMU from Xsens.

4-6-2 Multiple IMU cylinder configuration

It can also be observed that at lower angular velocities, the motion models using the angular acceleration outperform the angular velocity random walk model. This is to be expected as the accelerometers provide the least amount of information at lower angular velocities. It is then interesting to note that as the angular velocity magnitude gets higher, the angular velocity random walk model starts to outperform the angular acceleration motion models. Finally, it can be seen that even before $\omega \approx 300 \begin{bmatrix} 1 & 1 & 1 \end{bmatrix}^T$ rad/s, the Synthetic IMU starts to

outperform the Xsens gyroscope accuracy. The covariance estimates for the angular velocities are shown in Figure 4-8. The ratio with respect to the high-grade IMU can be seen in Table 4-2.

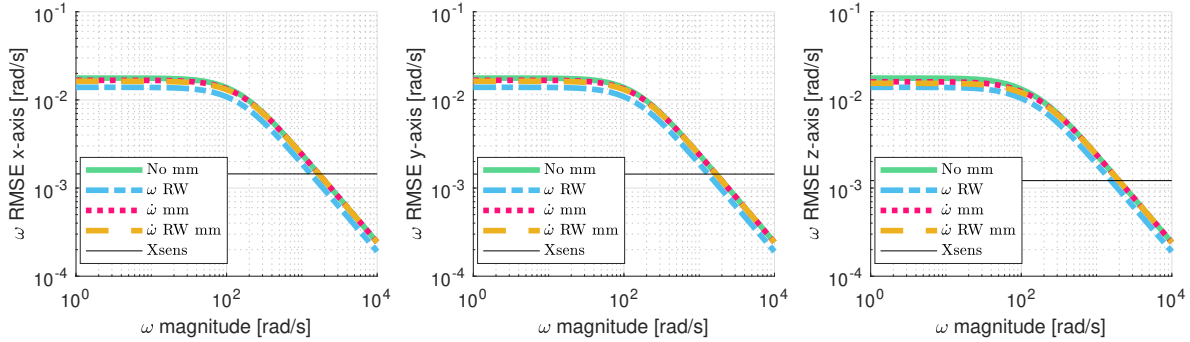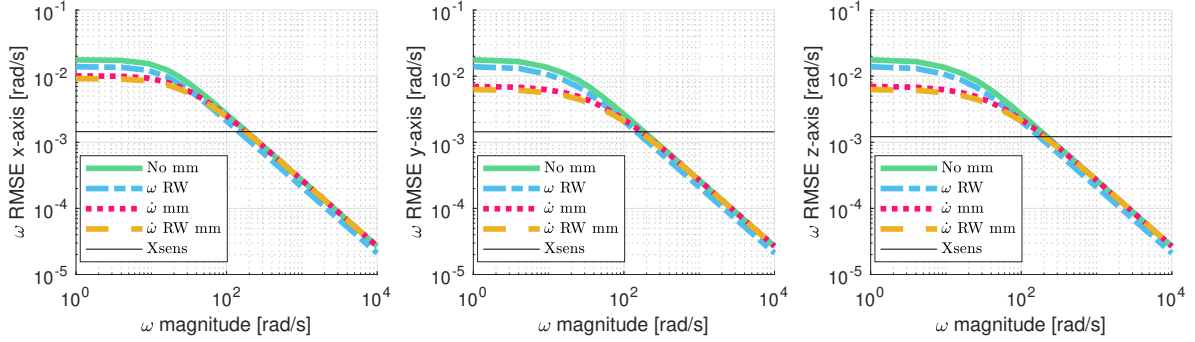**Figure 4-8:** Synthetic IMU angular velocity covariance after fusion of 16 IMUs placed on a cylinder. The covariances of the x-axis (left) y-axis (mid) and z-axis (right) using different motion models are shown, which are compared to MTi 300 IMU from Xsens.

The specific force covariance only dependends on the number of the accelerometer used and on the random walk models. There were 16 accelerometers used and the ratio of the covariance with respect to the high-grade IMU can be seen in Table 4-2.

motion model	Angular velocity in x- y- and z- axis [rad/s]				
Angular velocity	$\omega = 10^0$	$\omega = 10^1$	$\omega = 10^2$	$\omega = 10^3$	$\omega = 10^4$
ω no motion model	14.6	12.8	2.20	0.215	0.0220
ω random walk	11.4	10.1	1.73	0.169	0.0173
$\dot{\omega}$ motion model	8.32	7.69	2.07	0.215	0.0220
$\dot{\omega}$ random walk	7.55	7.00	2.07	0.215	0.0220
Specific force					
s no motion model	7.11				
s random walk	5.59				

Table 4-2: Performance comparison different motion models of the IMU cylinder. The performance is indicated by the ratio of the RSME with respect to the MTi 300 IMU from Xsens

4-7 Concluding remarks

4-7-1 Concluding remarks regarding the estimation of the CRLB of the MIMU4844 array

Influence of shifting the origin   The first effect is that when the Synthetic IMU shifts away from the origin, the covariance of the specific force starts to increase quadratically. For applications where all the sensors are used this probably will not pose a problem. This is because the origin of the Synthetic IMU can be chosen arbitrarily. It might pose a problem, however, when FDI is applied. When all the sensors on one side are assumed false and thus isolated, the origin is not in the same place as the centre of the remaining accelerometers. This will

lead to a loss in the accuracy of the specific force estimate. This was experienced during the simulation in Chapter 6 and the implications are elaborated on in that chapter.

Influence of the configuration The second interesting effect is that due to the configuration of the array, the covariance of the angular acceleration when adding more sensors scales linearly rather than quadratically. The same effect holds for the angular velocity, although this effect is not visible in Figure 4-2 as they add negligible information. This shows a 2D array is not the best configuration for estimating rotational motion. If the accelerometers were placed in a 3D array, where the accelerometers are equidistant in x- -y and z-direction, the covariance would start to decrease quadratically. This suggests that is is more important to optimize the distance between sensors in all directions rather than in a 2D plane. Instead of placing two layers of 16 IMUs on top of each other, more information can be obtained by placing 4 layers of 8 IMUs on top of each other.

Angular acceleration as a motion model A third interesting result regards the angular acceleration that can be used as a motion model prior for the angular velocity. The angular acceleration and the angular velocity both decrease quadratically with the distance between sensors squared. As both covariances decrease at the same rate, the ratio between the two remains constant. This suggests that the amount of information that the angular acceleration provides is independent of the configuration. While this is true for accelerometer-only arrays, the gyroscopes also provide information on the angular velocity. Starting around 10 times the scale factor, the accelerometers add enough information so that the angular velocity covariance starts to decrease. Before this point, the angular acceleration as a motion model will also provide less information. This shows that the benefit of bigger configurations is twofold. It is also apparent that as the angular velocity magnitude increases, the angular velocity covariance decreases while the angular acceleration covariance slightly increases. This shows that at lower angular velocities, the angular acceleration provides more information on the angular velocity as a motion model prior. This result has also been verified in [16].

4-7-2 Concluding remarks regarding the comparison against a higher-grade IMU

As the RMSE of the specific force of the IMU array and the cylinder when using a random walk model are about 46.3 times and 65.5 times larger than the accelerometer from Xsens. A lot more accelerometers be needed to get the same level of accuracy. Or more accurate accelerometers need to be used. Placing that many accelerometers in an array or on a human arm segment do not seem feasible.

The covariance of the angular velocity estimate, however, can compete with the high-grade IMU. The gyroscopes used for the array and the cylinder already perform better than the accelerometers (with respect to the high-grade IMU) but as the angular velocity increases, the accelerometers are also able to provide information on the estimate.

It must be said, however, that although the angular velocity random walk model outperforms the other motion models, in reality, this does not have to be the case. It was assumed here that the process noise was equal to the noise of the estimates. It would be reasonable to assume that the motion models using the angular acceleration as well have lower process noise than the angular velocity random walk model. These parameters would have to be tuned in reality depending on the application.

The results show that using more IMUs allow for a good estimate of the angular velocity. The motion models add a lot more information at lower angular velocities, in particular when use is made of the angular acceleration. Furthermore, at higher angular velocities a high accuracy estimate of the angular velocity can be obtained. This automatically extends to accelerometer-only arrays as the information of the accelerometers on the angular velocity outweigh the gyroscope information.

4-8   Answer to the research question

How can multiple lower-grade IMUs compare against a higher-grade IMU?

Chapter 5

Fault Detection and Isolation

In the previous two chapters assumed that the only errors in sensor measurements were either the bias or the white noise. It is more realistic, however, to assume that other faults may also potentially happen. Such a fault can be described as a disturbance. Using 3 or more sensors, which can be categorized as component redundancy, allows for Fault Detection and Isolation (FDI) [22, 25]. This chapter is focused on how a fault can be recognized and how it can be rejected. This Chapter is in parallel with Chapter 3 and builds further on Chapter 2. The assumption is made that all measurement noise is Gaussian, from this assumption a hypothesis test can be derived as shown in 5-1. Afterwards, in Section 5-2, the parity space method is introduced. Thereafter, in Section 5-3 a novel FDI application on MIMUs is introduced which builds on the work shown in Chapter 3. Finally, a INS is shown in Section 5-4.

5-1 Hypothesis Testing

If one wants to know whether a change has occurred or whether a fault is present it must be tested against a number of hypotheses. One of the more simplistic tests is the binary hypothesis test. The test takes on two hypothesis, the null hypothesis and the alternate hypothesis, which are expected to be true and false respectively. In case of fault detection the null hypothesis $\mathcal{H}_0$ would state that the fault is zero and the alternate hypothesis $\mathcal{H}_1$ states that there is no fault fault present [45]. This can be expressed as

$$\mathcal{H}_0 : \text{Fault is not present,} \tag{5-1a}$$

$$\mathcal{H}_1 : \text{Fault is present.} \tag{5-1b}$$

In order to reject the $\mathcal{H}_0$ or not reject $\mathcal{H}_0$ the following definitions are needed

- The detection probability : $P_D = P(\mathcal{H}_1|\mathcal{H}_1)$

- The correct rejection probability : $P_C = P(\mathcal{H}_0|\mathcal{H}_0)$

- The false alarm probability, or type I error : $P_{FA} = P(\mathcal{H}_1|\mathcal{H}_0) = 1 - P_C$

- The miss probability, or type II error : $P_M = P(\mathcal{H}_0|\mathcal{H}_1) = 1 - P_D$

To decide between the two hypothesis a likelihood ratio $\mathcal{L}(y)$ can be established as

$$\mathcal{L}(y) = \frac{p(y|\mathcal{H}_1)}{p(y|\mathcal{H}_0)} > \gamma, \tag{5-2}$$

where γ is the threshold can is chosen arbitrarily depending on the application. This rather simple hypothesis test is according to the Neymans-Pearson's lemma optimal [46] as it maximizes the detection probability P_D for a given false alarm rate P_{FA} [41]. Where P_{FA} is a function of γ. More specifically, one can set the false alarm probability to a fixed significance level such that γ can be found [47]

$$P_{FA} = \int_{y:\mathcal{L}(y)>\gamma} p(y|\mathcal{H}_0)dy = \alpha. \tag{5-3}$$

Two types of binary hypothesis are discussed in theory, the first is the simple hypothesis test, where a state can be either of two a priori known values. The second, known as composite hypothesis testing is where the state can take up an expected value or not that expected value. The second test is more realistic and is explained below.

5-1-1   Composite Hypothesis Testing

The composite hypothesis test considers two hypothesis. They null hypothesis $\mathcal{H}_0$, where the variable to be estimated takes up a known value and an alternative hypothesis $\mathcal{H}_1$, where the variable does not take up said value. This binary test is useful when one wants to test whether a fault is present or not. There are two common applications of this test. One is the Generalised Likelihood Ratio Test (GLRT) and the other is the Marginalised Likelihood Ratio Test (MLRT). Generally, one uses the MLRT when one wants to eliminate an unknown variable and GLRT when one can estimate the variable. Due to numerous sensors, a ML estimate can be found. The theory of composite hypothesis testing is shown below.

Consider the measurement given measurement model

$$y = Hx + e, \qquad e \sim \mathcal{N}(0, \Sigma), \tag{5-4}$$

where the matrix H maps the state space to the measurement space. The likelihood function is then given by

$$p(y|x) = \frac{1}{(2\pi)^{\frac{N}{2}}\sqrt{\det(\Sigma)}} \exp\left(-\frac{1}{2}(y - Hx)^T \Sigma^{-1}(y - Hx)\right). \tag{5-5}$$

The parameter x can take up an unknown value. The binary hypothesis test now takes the shape of

$$\mathcal{H}_0 : x = x_0, \tag{5-6a}$$

$$\mathcal{H}_1 : x \neq x_0. \tag{5-6b}$$

There are two major approaches to constructing a detector for such a hypothesis test [47], the former being the GLRT and the latter being Marginalization.

Generalised Likelihood Ratio Testing   The Generalised Likelihood Ratio Test simply put takes the ML estimate of x under $\mathcal{H}_1$, which from linear least squares is given by

$$\hat{x} = (H^T H)^{-1} H^T y, \tag{5-7}$$

and plugs this in as the value for x. This gives the following hypothesis test

$$\mathcal{L}(y) = \frac{p(y|x = \hat{x})}{p(y|x = x_0)}. \tag{5-8}$$

The resulting distributions are

$$2 \ln \mathcal{L}(y) \sim \begin{cases} \chi^2_{n_x}, & \mathcal{H}_0, \\ \chi^2_{n_x}((x_1 - x_0)^T I_{x_0}(x_1 - x_0)), & \mathcal{H}_1, \end{cases} \tag{5-9}$$

where I_{x_0} is the Fisher Information matrix under x_0.

5-2   Parity space method

One of the most used FDI method on IMUs is the parity space. The parity space method exists on two accounts, one is analytical redundancy and the other is component redundancy. The analytical redundancy refers to expressing past states towards the current state so that they can be compared. Component redundancy refers to having a multiplicity of the same measurement. Other than this difference, the method is the same for both applications.

The parity space is based upon GRLT as it creates a projection matrix that is orthogonal to the ML estimate state vector $\hat{x}$. The resulting vector is now free of the ML estimate state vector and is called the residual vector r. If no fault is present in the measurements, the residual vector contains only information upon erroneous measurements due to noise. If a fault is present then the parity vector contains information on noise and the fault. The parity space method is explained below

Consider the measurement equation and assume that the fault vector $F = 0$.

$$y = Hx + F + e, \qquad e \sim \mathcal{N}(0, \Sigma), \tag{5-10}$$

The MLE of is

$$\hat{x} = (H^T H)^{-1} H^T y. \tag{5-11}$$

Uising the MLE a projection matrix can be made as

$$\hat{y} = H\hat{x} = \underbrace{H(H^T H)^{-1} H^T}_{\mathcal{P}_\mathcal{H}} y, \tag{5-12}$$

where the projection matrix $\mathcal{P}_\mathcal{H}$ maps the measurement space into the expected measurement space based on the MLE. Furthermore, $\mathcal{P}_\mathcal{H}$ must adhere to $\mathcal{P}_\mathcal{H}^2 = \mathcal{P}_\mathcal{H}$ for it to be a projection matrix [45]. The prediction error can now be found as

$$\epsilon = y - \hat{y}, \tag{5-13}$$

which leads to the orthogonal projection matrix

$$\epsilon = \underbrace{(I - \mathcal{P}_H)}_{\mathcal{P}_{H_\perp}} y, \tag{5-14}$$

where $\mathcal{B}_{H_\perp}$ is of $\mathrm{rank}(\mathcal{P}_{H_\perp}) = n - \mathrm{rank}(H)$. It was shown, however, by [48] that due to the rank deficiency of the projection matrix $\mathcal{P}_{H_\perp}$, the prediction error vector is of lower rank and thus its covariance matrix can become non-singular. This can be circumvented by pre-multiplying the prediction error vector by the orthonormal basis $\mathcal{B}_{H_\perp}$. As was shown in [49] this is.

Furthermore, the projection matrix can also be constructed via the orthonomal basis $\mathcal{B}_{H_\perp}^T$ of the range space of H, denoted by $\mathcal{R}(H_\perp)$ [45]. The projection matrix can be constructed as

$$\mathcal{P}_{H_\perp} = \mathcal{B}_{H_\perp} \mathcal{B}_{H_\perp}^T. \tag{5-15}$$

it can be written in this form and to the fact that $\mathcal{B}_{H_\perp}^T \mathcal{B}_{H_\perp} = \mathcal{I}$, prediction error can be rewritten into the residual vector r [45]

$$r = \mathcal{B}_{H_\perp}^T r = \mathcal{B}_{H_\perp}^T \mathcal{B}_{H_\perp} \mathcal{B}_{H_\perp}^T y = \mathcal{B}_{H_\perp}^T y, \tag{5-16}$$

of which the co-variance is

$$\mathrm{cov}(r) = \mathcal{B}_{H_\perp}^T \Sigma \mathcal{B}_{H_\perp}. \tag{5-17}$$

By multiplying the residual by the square root of its covariance, the normalized residual has covariance identity. This is also known as whitening [49]. The normalized residual then takes the shape of

$$z = \underbrace{(\mathcal{B}_{H_\perp}^T \Sigma \mathcal{B}_{H_\perp})^{-\frac{1}{2}} \mathcal{B}_{H_\perp}^T}_{W} y. \tag{5-18}$$

From this another hypothesis can be made based whether the fault in (5-10) is zero or not, such that the null hypothesis is there is no fault and the alternative hypothesis states there is a fault.

$$\mathcal{H}_0 : z \sim \mathcal{N}(0, \mathcal{I}), \tag{5-19a}$$

$$\mathcal{H}_1 : z \sim \mathcal{N}(WF, \mathcal{I}). \tag{5-19b}$$

The Chi-square test statistic was derived similar to [45] as

$$\mathcal{L} \sim \begin{cases} \chi_\nu^2, & \mathcal{H}_0, \\ \chi_\nu^2 (F^T \mathcal{B}_{H_\perp} (\mathcal{B}_{H_\perp}^T \Sigma^{-1} \mathcal{B}_{H_\perp})^{-1} \mathcal{B}_{H_\perp}^T F)., & \mathcal{H}_1, \end{cases} \tag{5-20}$$

where $\nu = \mathrm{rank}(W) = \mathrm{rank}(\mathcal{P}_{H_\perp})$. From this distribution the a threshold can be chosen such that the null hypothesis can be rejected with a certain probability. In the chi-square test, when no fault is present the distribution takes the shape of the central chi-square distribution. If a fault is present, the distribution takes the shape of the non-central chi-square distribution. Both distributions can be seen in C-1.

5-3 Fault Detection and Isolation for Multiple IMUs

referentie naar aantal papers?

The parity space method has been used numerous times in IMU applications , however, to the knowledge of the writer, this is the first time it is used as an extension on the formulation in Section 3-4 by [14].

The application of FDI on MIMUs will be applied in two steps. In the first step, the linear parity space method as discussed in Section 5-2 is applied to the gyroscopes measurements only. It is of importance to eliminate faulty measurements first as these faulty measurements will influence the initial estimate. The estimate will then be used to remove the non-linear part from the stacked measurement equation (3-4c). For better FDI the initial estimate needs to be as close to the true angular velocity as possible.

The stacked observations (3-4c) is non-linear. The non-linear part, however, can be removed similar to Section 3-4, however, the assumption is now made that some sensors contain a fault. Under this assumption, the fusion of all measurements would lead to a biased ML estimate. Instead of using the Gauss-Newton optimization to find the angular velocity, use of a prior from the motion model as described in Section 3-5 can be made.

Simultaneously, the parity space method can also be applied to gyroscope measurements alone. It is assumed that the prior $\hat{\tilde{\omega}}$ and the healthy gyroscope measurements are now only corrupted by white noise. It is also assumed that all the estimates of the angular velocity are independent of each other. The estimates of the angular velocity estimates are distributed as

$$\hat{\tilde{\omega}} \sim \mathcal{N}(\tilde{\omega}, \Sigma_{\tilde{\omega}}),$$
$$y_{\omega,i} \sim \mathcal{N}(\omega, Q_{\omega,i}).$$

Where $i = 1 : N_{\omega,\text{healthy}}$ denotes the healthy gyroscopes. A fused estimate of the angular velocity at a time instance can be found by taking the WLS as [41]

$$\hat{\omega} = \left(\Sigma_{\tilde{\omega}}^{-1} + \sum_{i=1}^{N_{\omega,\text{healthy}}} Q_{\omega,i}^{-1} \right)^{-1} \left(\Sigma_{\tilde{\omega}}^{-1} \hat{\tilde{\omega}} + \sum_{i=1}^{N_{\omega,\text{healthy}}} Q_{\omega,i}^{-1} y_{\omega,i} \right). \tag{5-22}$$

After the faulty gyroscopes have been identified, the weighted average of the gyroscopes can be taken for an estimate of the angular velocity. This leads to two independent estimates of the angular velocity, which can be fused to remove the non-linear part $h(\omega)$ from the measurement space.

In is assumed that the estimate of the angular velocity close enough to the true angular velocity. The adapted measurement equation has covariance $R = H(H^T Q^{-1} H)^{-1} H^T + Q$, as was shown in Section ?? and takes the form of

$$Y - h(\hat{\omega}_0) = H\hat{\theta} + E. \tag{5-23}$$

The parity space method as discussed in Section 5-2 can now be applied to the previous adapted measurement equation. The method is summarized in Algorithm 5.

Algorithm 5: A novel parity space method for Multiples IMUs to identify faulty measurements

---

Run FDI scheme for gyroscope measurements, set $T_\omega = 1$;

while $T_\omega = 1$ **do**

$$
\begin{aligned}
\mathcal{B}_{H_{\omega,\perp}} &= \text{null}(H_\omega^T), \\
\nu_\omega &= \text{rank}\left(\mathcal{B}_{H_{\omega,\perp}}\right), \\
r_\omega &= \left(\mathcal{B}_{H_{\omega,\perp}}^T \mathcal{B}_{H_{\omega,\perp}}\right) Y_\omega, \\
z_\omega^T z_\omega &= Y_\omega^T \mathcal{B}_{H_{\omega,\perp}} \left(\mathcal{B}_{H_{\omega,\perp}}^T Q_\omega \mathcal{B}_{H_{\omega,\perp}}\right)^{-1} \mathcal{B}_{H_{\omega,\perp}}^T Y_\omega.
\end{aligned}
$$

Run hypothesis test on $z_\omega^T z_\omega \sim \chi^2_{\nu_\omega}$ to update T_ω ;

if $T_\omega = 1$ **then**

   find sensor with highest residual in vector r_ω ;
   remove said sensor from measurements ;

end

end

Run FDI scheme for accelerometer + gyroscope measurements ;

$$
\hat{\omega} = \left(\Sigma_{\tilde{\omega}}^{-1} + \sum_{i=1}^{N_{\omega,\text{healthy}}} Q_{\omega,i}^{-1}\right)^{-1} \left(\Sigma_{\tilde{\omega}}^{-1}\hat{\tilde{\omega}} + \sum_{i=1}^{N_{\omega,\text{healthy}}} Q_{\omega,i}^{-1} y_{\omega,i}\right).
$$

while $T = 1$ **do**

$$
\begin{aligned}
\mathcal{B}_{H_\perp} &= \text{null}(H^T), \\
\nu &= \text{rank}\left(\mathcal{B}_{H_\perp}\right), \\
r &= \left(\mathcal{B}_{H_\perp}^T \mathcal{B}_{H_\perp}\right)(Y - h(\hat{\omega})), \\
z^T z &= (Y - h(\hat{\omega}))^T \mathcal{B}_{H_\perp} \left(\mathcal{B}_{H_\perp}^T R \mathcal{B}_{H_\perp}\right)^{-1} \mathcal{B}_{H_\perp}^T (Y - h(\hat{\omega})).
\end{aligned}
$$

Run hypothesis test on $z^T z \sim \chi^2_\nu$ to update T ;

if $T = 1$ **then**

   find sensor with highest residual in vector r ;
   remove said sensor from measurements ;

end

end

5-4 Fault Detection and Isolation with Multiple IMUs Inertial Navigation Solution

Two INS schemes have been shown earlier in Section 2-5 and Section 3-7 where a navigation solution was shown for a single IMU and Multiple IMUs respectively. In this chapter, a novel method for FDI was introduced which allows for the detection and isolation of faulty sensors. This takes place after the sensors are pre-processed and before they are fused together into a Synthetic IMU. Use is made of the motion model prior not only improves the estimate of the angular velocity needed for FDI, but also allows for this FDI method to be applied to accelerometer-only arrays. The new navigation solution is shown in Figure 5-1 where the are enclosed by the green rectangle shows how FDI can be implemented into the previous navigation solutions.
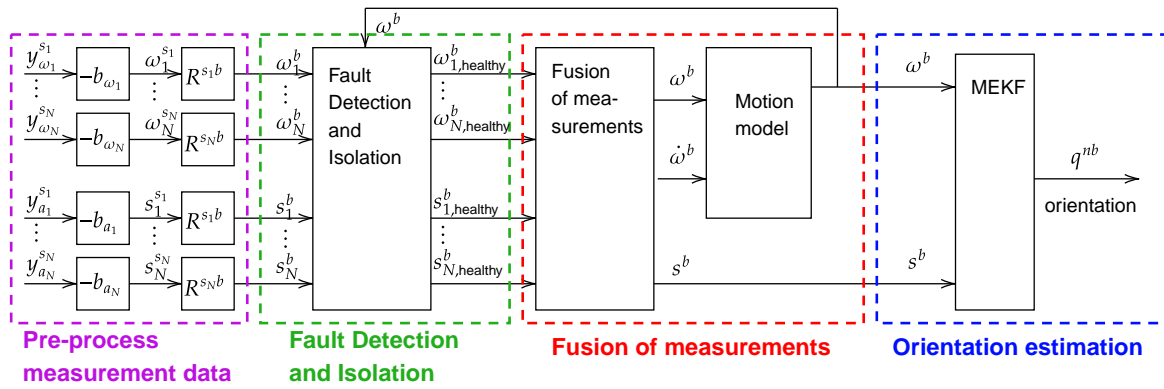

Figure 5-1: A Strapdown Inertial Navigation scheme using Multiple gyroscopes and accelerometers and FDI. The measurement data is first pre-processed in the purple rectangle after which in the green rectangle faulty sensors are removed. The remaining healthy sensors are fused into a Synthetic IMU in the red rectangle. The synthetic IMU then estimates the pose in the blue rectangle.

Fault Detection and Isolation Simulation Setup and Results

This Chapter will test the novel parity space method as presented in 5-3. In Section 6-1 the simulation setup for the cylinder, how the simulation data is generated and how the disturbance is simulated is discussed. Afterwards, in **??** the results of the simulation are shown. In the results, first, the states are shown and to what extent the disturbance can be rejected, afterwards how the covariance of the specific force is affected is shown. Finally, it is shown how the orientation estimation is affected by the disturbance.

6-1 Simulations to test FDI

In Chapter 2 it was shown how a navigation solution can be found using angular velocity and specific force estimates. Afterwards in Chapter 3 it was shown how multiple IMUs can be fused into a single synthetic IMU finally in Chapter 5 a novel parity space method to detect and isolate faulty sensors was proposed. How everything combines is summarized in Figure 5-1. In this simulation, the novel parity space method will be tested with a MC simulation using 100 data realizations.

Simulation setup for a cylinder   Previously, the capabilities of placing IMUs in an array and placing IMUs on a cylinder were analyzed. Here, the simulation continues on the cylinder in the shape and size of a human arm segment. The cylinder is $0.3m$ long and has a radius of $0.05m$, the IMUs are placed equidistantly and can be seen in Figure 4-6. It is assumed that biases and misalignment errors can be calibrated for properly. It is also assumed that the positions can be calibrated for properly. The covariances of the accelerometers and gyroscopes are normally distributed with covariances matrices

$$\Sigma_{a_i} = \begin{bmatrix} 0.4 & 0 & 0 \\ 0 & 0.4 & 0 \\ 0 & 0 & 0.4 \end{bmatrix}, \qquad \Sigma_{\omega_j} = \begin{bmatrix} 0.1 & 0 & 0 \\ 0 & 0.1 & 0 \\ 0 & 0 & 0.1 \end{bmatrix}, \tag{6-1}$$

for $i = 1 : 16$ accelerometers and $j = 1 : 16$ gyroscopes.

Simulation data   The simulation of measurement data was done as described in Section 4-3 and summarized in Algorithm 6 in Appendix E. The linear acceleration was set at 0 m/s. Instead of setting the angular velocity to arbitrary values, a random walk model for an angle ϕ^b was generated. The angle ϕ is saturated between $\phi = \pm \begin{bmatrix} \pi/5 & \pi/5 & \pi/5 \end{bmatrix}^T$ so that wrapping issues in the results are minimized. Afterwards, the angle was smoothed using a moving average filter in to remove the erraticness of the data. The angular velocity can be calculated from this angle as the first order discrete time derivative. The simulation of this data is as

$$\phi^b_{k+1} = \phi^b_k + e_{\phi,k}, \tag{6-2a}$$

$$\omega^b_{k+1} = \frac{\phi^b_{k+1} - \phi^b_k}{T}. \tag{6-2b}$$

Simulating a disturbance   One of the problems in motion capture for humans is disturbances caused by hitting or banging against an object. This will cause a spike in the accelerometer readings resulting in erroneous measurements. As the surface of the arm is soft tissue, the disturbance should be the largest at the point of contact of where the arm would hit an object. The magnitude of the disturbance should dissipate along the length of the arm. The disturbance is simulated as a dampened harmonic oscillation and the magnitude of the disturbance is shown in Figure 4-6. The disturbance will be applied in the y-axis and the z-axis of the body frame. See Section **??** in the Appendix for details on how the disturbance is simulated.
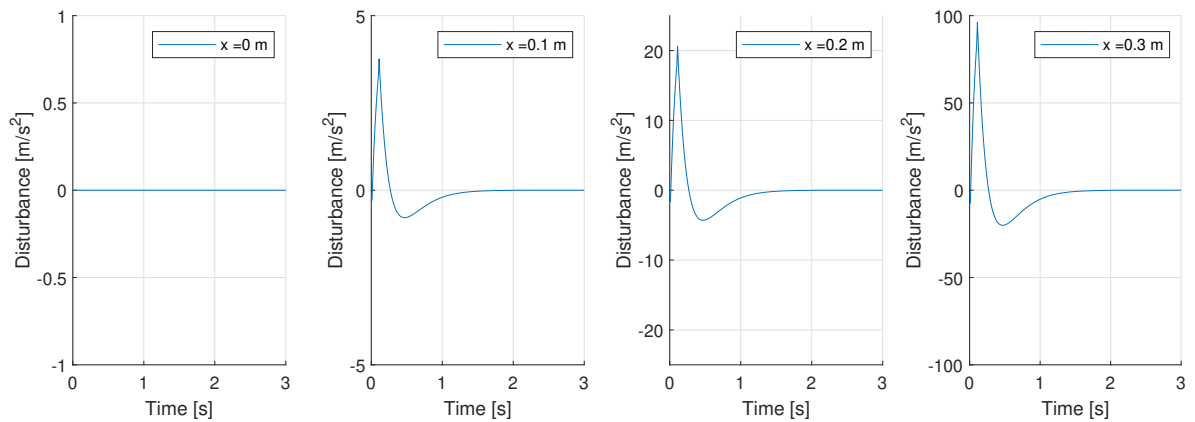
> Iets meer ingaan op dit probleem

Figure 6-1: Disturbance in acceleration for different positions along the x-axis of the cylinder as in Figure 4-6.

A short summary on the INS solution   To analyze the parity space method the INS scheme in Section 5-4 is used. The first step here is to pre-process the data, however, as it is assumed that the measurements do not have a bias and are not prone to misalignment errors, this step can be disregarded. The measurement data at this point is in the individual sensor frames and first must be rotated into the body frame. Afterwards, the data in the body frame can be tested against each other using the novel parity space method described in Section 5-3, where use is made of a prior on the angular velocity to determine faulty sensors. The remaining healthy sensors can then be fused into a Synthetic IMU and use of the angular acceleration can be made to obtain a new angular velocity prior. Finally, the synthetic IMU can be used to obtain the orientation estimation in the MEKF.

6-2   Results

The results are shown in the subsections below, first the states are shown and to what extent the disturbance applied influences the estimate of the states. Afterwards, the covariance of the specific force is shown and how it is impacted by the location of where the Synthetic IMU is fused. Afterwards, the orientation estimation is shown to analyze the impact on the orientation.

6-2-1   Rejecting disturbance

A MC simulation of 100 realizations was done with the disturbance as in Figure 6-1. Most of the disturbance can be rejected using the parity space method, the results on the states are shown below.

Angular velocity   The angular velocity states can be seen in Figure 6-2 and the error of the states can be seen in Figure 6-3. During the disturbance, the fused angular velocity of the Synthetic IMU without FDI takes on an error. At its peak the error in the x-axis takes on almost $0.15 rad/s$. The accelerometers undergoing a minor disturbance are not identified as faulty sensors. As such, the disturbance still influences the angular velocity estimate when fusing the sensors into a Synthetic IMU.

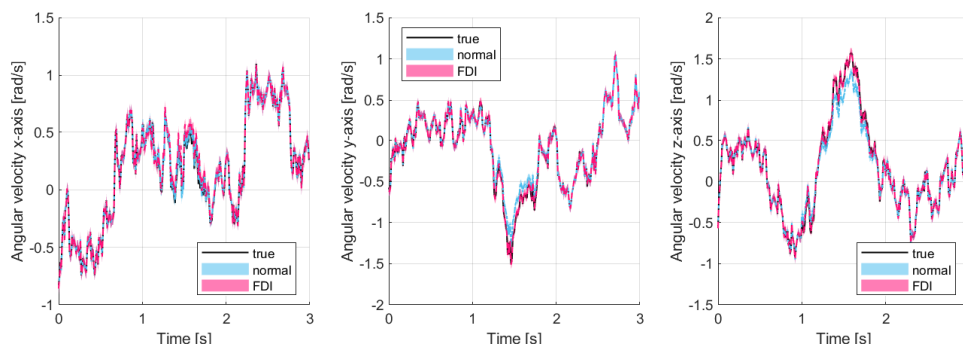> welke accelerometers fout zijn ook nog laten zien?

Figure 6-2: True angular velocity states (black) and mean angular velocity states of the synthetic IMU with (blue) and without (pink) FDI using 100 MC realizations for the x-axis (left), y-axis (mid) and z-axis (right) of the body frame.

Figure 6-3: Mean angular velocity errors of the synthetic IMU with (blue) and without (pink) FDI using 100 MC realizations for the x-axis (left), y-axis (mid) and z-axis (right) of the body frame.

Angular acceleration In Figure 6-4 and Figure 6-5 the angular acceleration states and errors can be seen respectively. The angular acceleration is disturbed significantly when no FDI is applied, however, most of the error can be nullified using FDI. Some of the error still remains as some of the accelerometers that are deemed healthy still undergo a small disturbance.

Figure 6-4: True angular acceleration states (black) and mean angular acceleration states of the synthetic IMU with (blue) and without (pink) FDI using 100 MC realizations for the x-axis (left), y-axis (mid) and z-axis (right) of the body frame.
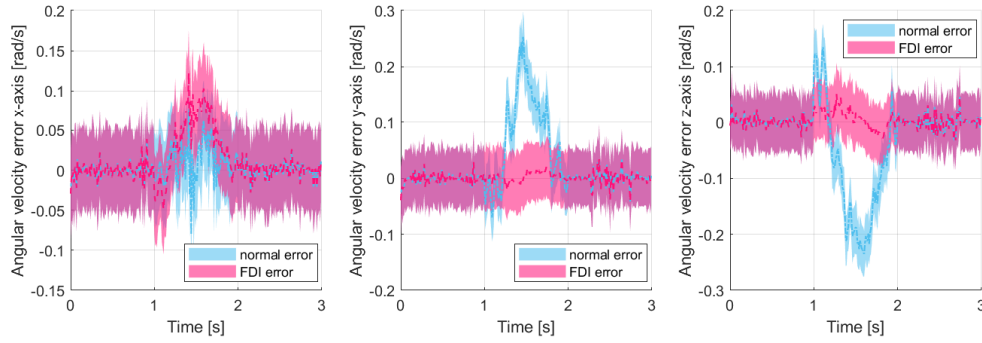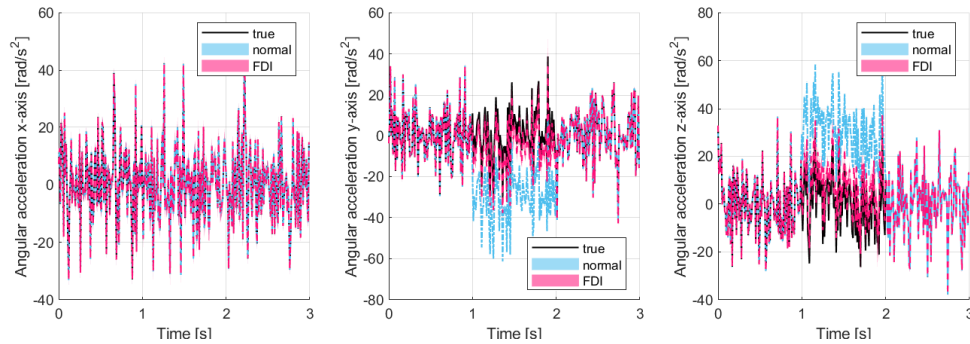
Figure 6-5: Mean angular acceleration errors of the synthetic IMU with (blue) and without (pink) FDI using 100 MC realizations for the x-axis (left), y-axis (mid) and z-axis (right) of the body frame.

Specific force The states of the specific force and the complementary errors are shown in Figure 6-6 and Figure 6-7 respectively. At the time of the disturbance, the y-axis and z-axis of the Synthetic IMU without FDI undergo a maximum error of 30 m/s and 20 m/s respectively, the x-axis does not undergo the disturbance. This is to be expected as the direction of the disturbance was applied in the direction the y-axis and the z-axis of the body frame. The Synthetic IMU that does undergo FDI can reject most of the disturbance in the y-axis and z-axis. Interestingly, this does cause a small error in the x-axis.

Figure 6-6: True specific force states (black) and mean specific force states of the synthetic IMU with (blue) and without (pink) FDI using 100 MC realizations for the x-axis (left), y-axis (mid) and z-axis (right) of the body frame.
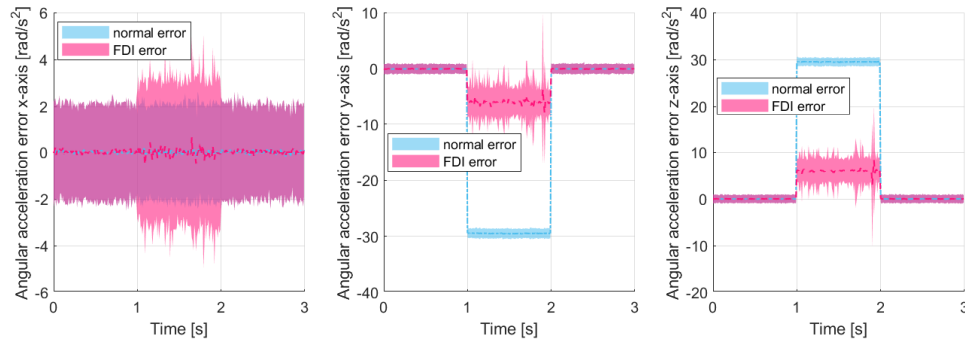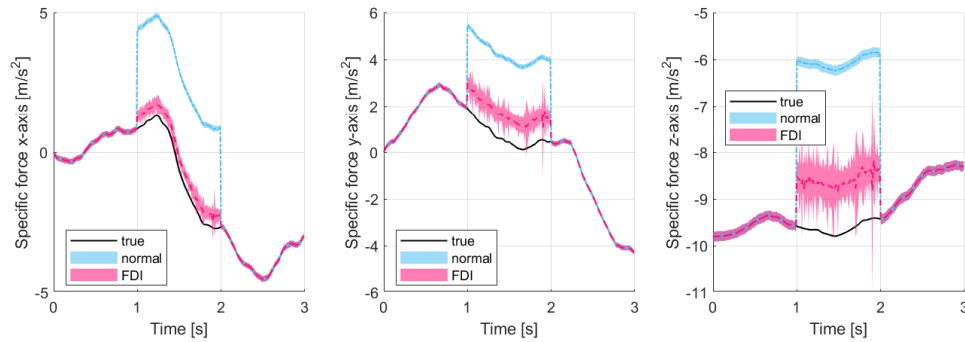
Figure 6-7: Mean specific force errors of the synthetic IMU with (blue) and without (pink) FDI using 100 MC realizations for the x-axis (left), y-axis (mid) and z-axis (right) of the body frame.
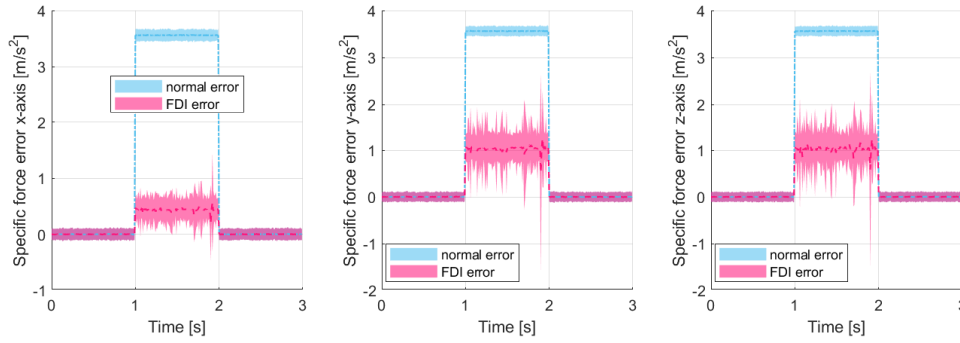
6-2-2   Specific force covariance

During the disturbance, most of the accelerometers are rejected as faulty measurements and are, therefore, not taken into account when fusing the measurements together. Due to the nature of the disturbance, however, the accelerometers that are left are all on one side of the cylinder. This causes the origin to be displaced away from the center of the accelerometers. This effect was shown earlier in Section 4-4-3. There, an analysis was done the CRLB and the displacement of the origin. When the origin displaces itself from the center of the accelerometers, the covariance of the specific force increases. Both covariances are plotted in Figure 6-8.
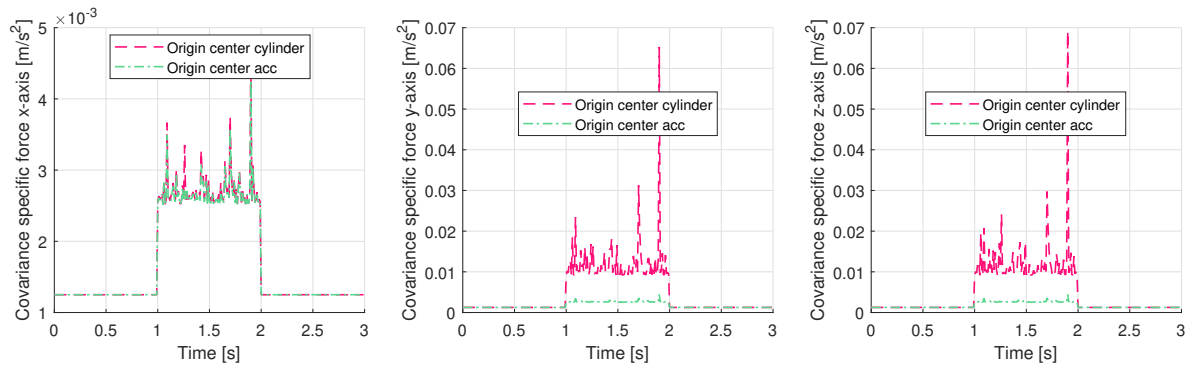
Figure 6-8: MC simulation of 100 realizations with an applied disturbance. The x-axis (left), y-axis(mid) and z-axis (right) covariances of the specific force of the Synthetic IMU is shown when the origin is in the centre of the cylinder (pink) and when the origin is in the centre of the healthy accelerometers (green).

The uncertainty on the specific force has now increased by such an amount that the measurement update in the MEKF has negligible effect. The can be solved by changing the origin from the centre of the cylinder towards the the center of the healthy accelerometers. The assumption is then made that a rigid body is used and thus the linear and rotational motion should be the same for every point in the rigid body. Thus, if the origin of the Synthetic IMU is placed on any part of the rigid body the covariance estimate should be valid.

6-2-3 Orientation estimation

The simulation results of the true data, no FDI method and the parity space method is seen in Figure 6-9. For all Synthetic IMUs, the roll and pitch angle converge back towards the true angles due to the gravity vector. The gravity vector, however, does not provide any information on the yaw angle. Therefore, in the aftermath of the disturbance, the yaw angles may experience a constant offset from the true angle.

Synthetic IMU without FDI It can be observed that at the time of the disturbance, when not using the parity space method (blue), the roll angle undergoes a large error which peaks at about $-340°$. The pitch angle error, which peaks at about $20°$ while the yaw angle error peaks at about $-65°$. This error can be partially attributed to the error in the estimate of the angular velocity, but also to the violation of the assumption the the specific force is almost equal to the gravity vector.

Synthetic IMU with FDI (pink) It can also be observed that when applying FDI (pink), the pitch angle undergoes a significant error. The angular velocity estimates are impacted by the disturbance and deviate from the true angular velocity causing drift in the pitch angle. The specific covariance relatively high, so the measurement update in the MEKF has no significant impact on the orientation estimation.

Synthetic IMU with FDI (green) Finally, for the Synthetic IMU with the origin at the centre of the healthy accelerometers (green), the disturbance is rejected and the angle does not drift away from the true angle. As the origin of the Synthetic IMU is now placed in the centre of the healthy accelerometers, the specific force is accurate enough such that the measurement update in the MEKF has a significant effect.

Figure 6-9: MC simulation of 100 realizations with an applied disturbance. The Synthetic IMUs undergo no FDI (blue), and undergo FDI (pink and green). Pink has the origin at the centre of the cylinder and green at the centre of the accelerometers. The estimated and true angles (left) and the error of the angles (right) are the roll (top), pitch (mid) and yaw(bottom).
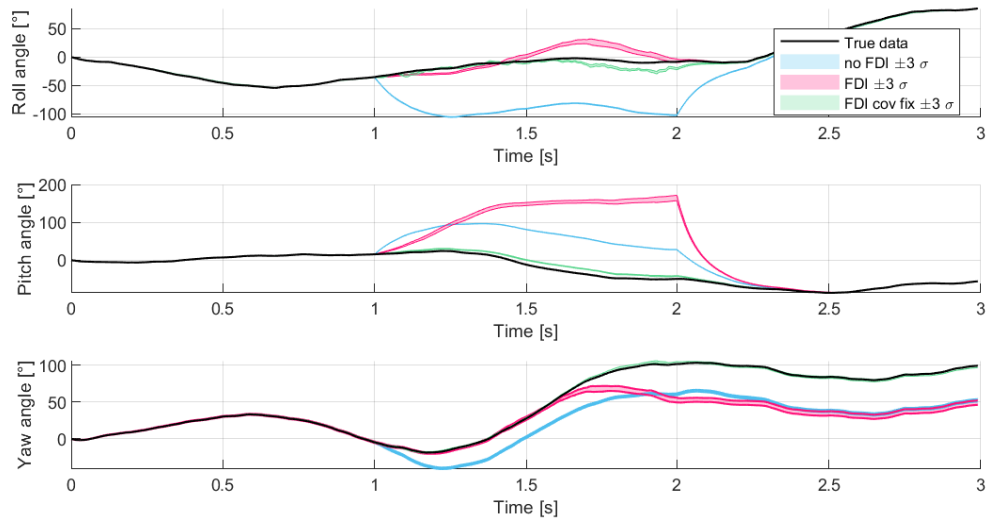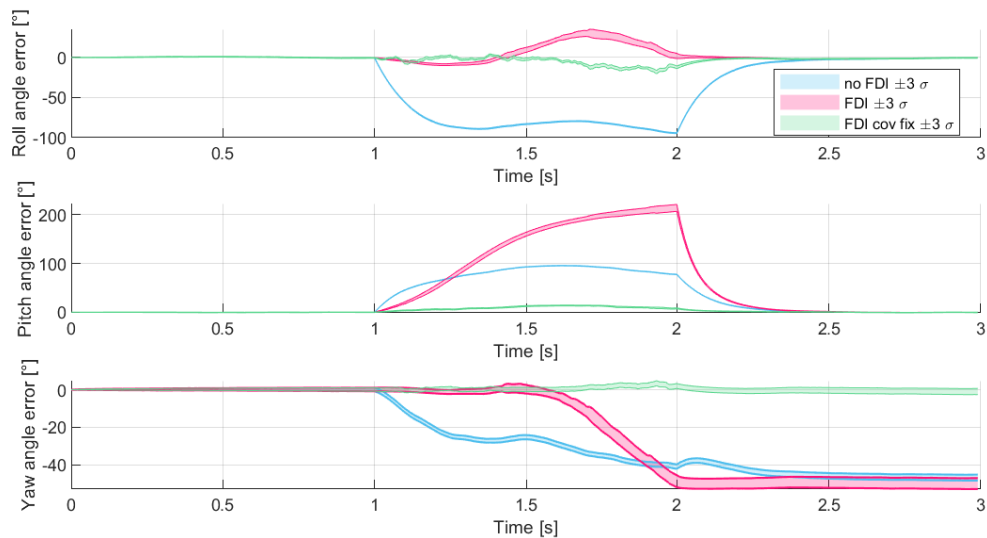
Caption

Figure 6-10: MC simulation of 100 realizations with an applied disturbance. The Synthetic IMUs undergo no FDI (blue), and undergo FDI (pink and green). Pink has the origin at the centre of the cylinder and green at the centre of the accelerometers. The estimated and true angles (left) and the error of the angles (right) are the roll (top), pitch (mid) and yaw(bottom).
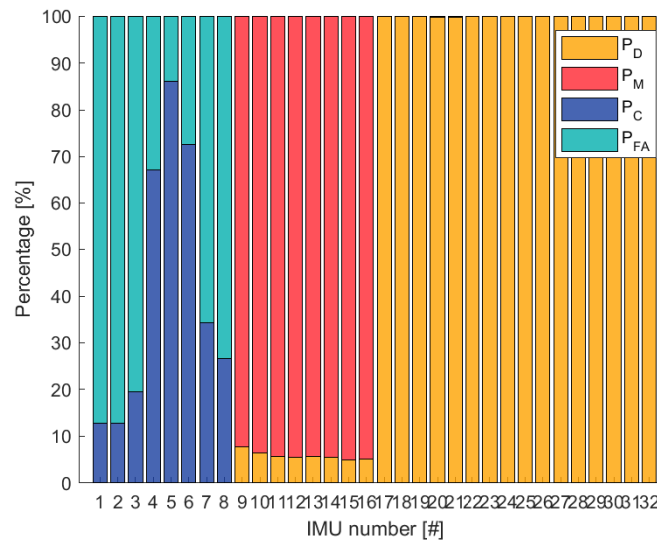
Figure 6-11: MC simulation of 100 realizations with an applied disturbance.
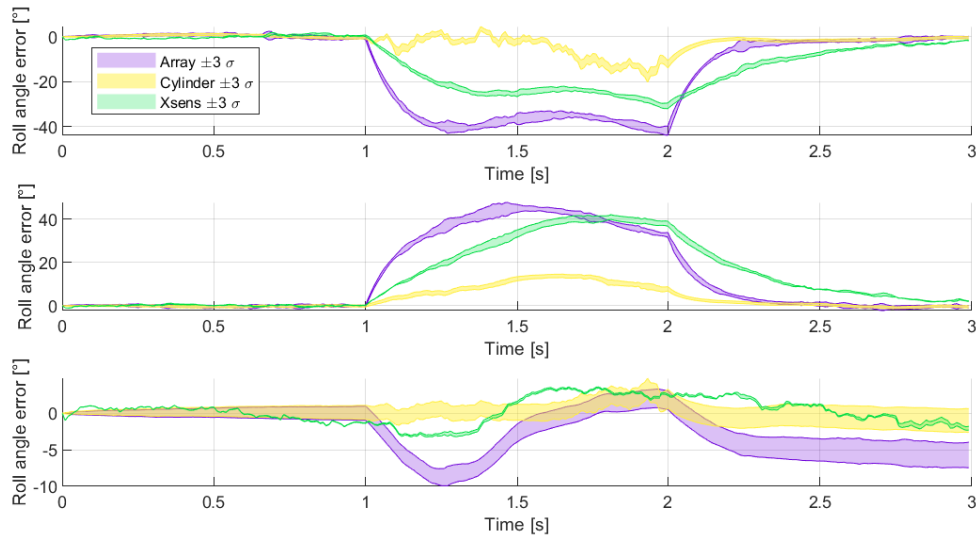
Figure 6-12: MC simulation of 100 realizations with an applied disturbance.

A short conclusion   From the results of the states, it can be observed that most of the disturbance gets rejected properly. With Fusing all the measurements at the centre of the healthy accelerometers, the specific force covariance is accurate enough to add enough information towards our belief of the orientation. From these results, it can be concluded that the novel parity space method is effective against disturbances in simulation. It remains to been seen, however, how it will hold up in reality.

Chapter 7

Discussion and Conclusion

7-1 Short summary on the relevant results

Placeholder

7-2 Caveats on the novel parity space method

In the current simulation it is assumed that when the accelerometers hit an object, they only undergo a spike in their measurements. In reality, however, it would be more realistic to assume that the accelerometers experience some displacement and or rotation. These changes in orientation and position on the IMUs would influence future measurement readings that are not taken into account int the current model. This can potentially be resolved by introducing a prior on the measurement covariance matrix of the IMU which has been disturbed for future time steps. The covariance matrix would not only include white noise but would also have to model the other sensor errors.

It is also realistic to assume that when an IMU on one part of the body is determined to be faulty, IMUs that are close to the faulty IMU are more likely to be faulty as well. This knowledge can be used in the form of a prior as well. The IMUs that are close to the faulty IMU can be given a prior on their covariance matrix, for the current and future states, such that it includes other errors than white noise.

Accelerometers and gyroscopes are usually combined into a single IMU, hence if an accelerometer experiences a disturbance, it would be likely that the gyroscopes are disturbed as well. In the current simulation, this has not been taken into account as it was assumed that the gyroscopes can be placed anywhere. If the accelerometer and gyroscope are combined into a single IMU and one of the two is deemed to be a faulty sensor, it could be reasonable to

assume that the entire IMU is faulty.

In the current form, where all measurements are fused to form a Synthetic IMU it is not possible to use external measurements such as GPS for FDI. To test the individual IMUs for faults using GPS the individual navigation solution has to be found, then it can be fused into a Synthetic IMU. This is a considerable downside of the parity space method where only use is made of the ML estimate.

Throughout the simulations, it has been assumed that the biases were constant and could be compensated for. It might be more realistic to assume that the biases are time-varying and in the current form cannot be included in the state space. The INS scheme would have to be altered slightly such that the fusion of measurements into a synthetic IMU and the motion models are included into the MEKF. Note that this has been implemented by [8] also based on the works of [14], where use was made of an IMU array.

7-3 Future Work

The FDI method shown in the thesis has only been shown to work in simulation, it remains to be seen, however, if it will hold up in a real-life scenario. The method first must be validated in a real-life experiment.

The current parity space method is based solely on the ML estimate of the current time step. A MAP estimate can be found by including motion models of the specific force and the angular acceleration. It could be interesting to see how these motion models affect the ability to accurately identify faulty measurements.

Whenever a sensor is continuously faulty they can be either left out. It would be likely to assume that the IMU has been either displaced or has been rotated. It could be possible to re-calibrate for the position and orientation error so that in the future the sensor is deemed healthy again. Another, easier approach, could be to increase the covariance matrix of the faulty sensor such that the fault can be modeled as well.

The work explained in [8] is similar to the work presented here, however, there no use is made of FDI. Instead, the fusion of measurement was Incorporated into an Iterative Extended Kalman Filter. Furthermore, the addition of gyro-bias tracking, a bandpass filter as a model for the linear acceleration. They also added a two-speed attitude integration architecture was used to increase computational efficiency. The parity space method presented in in this thesis can be used in its current form with their work as well.

7-4 Conclusion

Answer the research questions...

Appendix A

A-1 Orientation Paramaterizations

A-1-1 Euler angles

Building on rotation matrices, Euler angles are three consecutive rotation matrices around specified axes. Different Euler angle parameterizations are possible, one of them is by looking at three consecutive rotations, yaw, pitch and roll (ψ, θ, ϕ) around the (z, y, x) axes respectively. The rotation R^{bs} is thus $R^{bs} = R^{bs}(\phi)R^{bs}(\theta)R^{bs}(\psi)$ which can be expressed as

$$
R^{bs} = \underbrace{\begin{bmatrix} 1 & 0 & 0 \\ 0 & \cos(\phi) & \sin(\phi) \\ 0 & -\sin(\phi) & \cos(\phi) \end{bmatrix}}_{R^{bs}(\phi)} \underbrace{\begin{bmatrix} \cos(\theta) & 0 & -\sin(\theta) \\ 0 & 1 & 0 \\ \sin(\theta) & 0 & \cos(\theta) \end{bmatrix}}_{R^{bs}(\theta)} \underbrace{\begin{bmatrix} \cos(\psi) & \sin(\psi) & 0 \\ -\sin(\psi) & \cos(\psi) & 0 \\ 0 & 0 & 1 \end{bmatrix}}_{R^{bs}(\psi)}, \tag{A-1}
$$

or when written as a single matrix it is given as

$$
R^{bs} = \begin{bmatrix} \cos(\theta)\cos(\psi) & \cos(\theta)\sin(\psi) & -\sin(\theta) \\ \sin(\phi)\sin(\theta)\cos(\psi) - \cos(\phi)\sin(\psi) & \sin(\phi)\sin(\theta)\sin(\psi) + \cos(\phi)\cos(\psi) & \sin(\phi)\cos(\theta) \\ \cos(\phi)\sin(\theta)\cos(\psi) + \sin(\phi)\sin(\psi) & \cos(\phi)\sin(\theta)\sin(\psi) - \sin(\phi)\cos(\psi) & \cos(\phi)\cos(\theta) \end{bmatrix}. \tag{A-2}
$$

As the Euler angles are based on the Rotation matrices the same properties hold and thus the Euler angles are also in SO(3). Contrary to rotation matrices, however, Euler angles are prone to singularities and are not unique in describing rotations. A phenomenon called gimbal lock can take place which is when two rotations describe the same rotations around an axis [30, 5]. Another problem that is frequent with Euler angles is that wrapping also induces non-uniqueness.

A-1-2 Rotation vectors

Every rotation can be described by a single rotation around a single axis. This rotation can be expressed as a normalized unit vector n which lies in the group $\mathbb{S}^2$ with a rotation angle

α in $\mathbb{R}$. A mapping can be made that maps the axis-handle from representation into $SO(3)$ [29]. This mapping can be denoted by $\exp(-\alpha[n\times])$.

The rotated vector x_* can be expressed in terms of the original vector x, a rotation α and a normalized vector n as

$$x_* = x\cos\alpha + n(x \cdot n)(1 - \cos\alpha) - (n \times x)\sin\alpha, \tag{A-3}$$

where a detailed derivation can be found in [5]. By introducing the notation $[x\times]$ allows one to write the skew-asymmetric matrix as

$$[x\times] \triangleq \begin{bmatrix} 0 & -x_3 & x_2 \\ x_3 & 0 & -x_1 \\ -x_2 & x_1 & 0 \end{bmatrix}. \tag{A-4}$$

Given 3 arbitrary vectors u, v and w, multiple cross products can be expressed as terms of dot products as

$$u \times (v \times w) = v(w \cdot u) - w(u \cdot v). \tag{A-5}$$

Combining equations (A-4) and (A-5) with (A-3) allows one to rewrite the rotation vector as

$$x_* = (\mathcal{I}_3 - \sin\alpha[n\times]) + (1 - \cos\alpha)[n\times]^2)x, \tag{A-6}$$

leading to the compact expression of

$$x_* = \exp(-\alpha[n\times])x. \tag{A-7}$$

Which is an equivalent to a rotation matrix if it were parameterized in terms of α and n [5]. There is, however, a problem that arises when using rotation matrices. The problem is that some rotation cannot be described by the axis-handle paramaterization. By looking at the inverse mapping which is given by (tr is the trace operator)

$$\alpha = \cos^{-1}(\frac{1}{2}(\mathrm{tr}(R) - 1)), \tag{A-8a}$$

$$n = \frac{1}{2\sin(\alpha)} \begin{bmatrix} R_{32} - R_{23} \\ R_{13} - R_{31} \\ R_{21} - R_{12} \end{bmatrix}, \tag{A-8b}$$

it can be observed that when $\sin(\alpha)$ goes to 0 the unit vector n goes to infinity. Thus the axis-handle parameterization becomes invalid for angles $\alpha = k\pi$, for $k = 0, 1, ...$ [30].

A-1-3   Quaternions

A unit quaternion is an orientation parameterization in $q \in \mathbb{R}^4$, however, in reality, orientation is in $\mathbb{R}^3$. This means in order to use the quaternions we must exploit a trick such that our coordinate vector can be rewritten as follows

$$\bar{x}^s = \begin{bmatrix} 0 \\ x^s \end{bmatrix}. \tag{A-9}$$

A rotation with unit quaternions is defined as

$$\bar{x}^b = q^{sb} \odot \bar{x}^s \odot (q^{sb})^c, \tag{A-10}$$

where $(q^{sb})^c$ denotes the complex conjugate of the unit quaternion, defined as

$$\begin{bmatrix} q_0 \\ q_v \end{bmatrix}^c = \begin{bmatrix} q_0 \\ -q_v \end{bmatrix}. \tag{A-11}$$

The quaternion multiplication $\odot$ is denoted by

$$p \odot q = \begin{bmatrix} p_0 q_0 - p_v \cdot q_v \\ p_0 q_v + q_0 p_v + p_v \times q_v \end{bmatrix} = p^L q = q^R p, \tag{A-12}$$

where

$$p^L \triangleq \begin{bmatrix} p_0 & -p_v^T \\ p_v & p_0 \mathcal{I}_3 + [p_v \times] \end{bmatrix}, \qquad p^R \triangleq \begin{bmatrix} p_0 & -p_v^T \\ p_v & p_0 \mathcal{I}_3 - [p_v \times] \end{bmatrix}. \tag{A-13}$$

Combining (A-4) and (A-13) into (A-10) results into the following

$$\bar{x}^b = (q^{bs})^L (q^{sb})^R \bar{x}^s = \begin{bmatrix} 1 & 0_{1x3} \\ 0_{3x1} & q_v q_v^T + q_0^2 \mathcal{I}_3 + 2q_0 [q_v \times] + [q_v \times]^2 \end{bmatrix} \begin{bmatrix} 0 \\ x_v \end{bmatrix}, \tag{A-14}$$

By taking the axis-handle representation and rewriting it in quaternion form, one can choose to express it as follows

$$q^{bs}(n^s, \alpha) = \begin{bmatrix} \cos(\frac{\alpha}{2}) \\ -n^s \sin(\frac{\alpha}{2}) \end{bmatrix}, \tag{A-15}$$

such that (A-14) can be written in the form of

$$\bar{x}^b = \begin{bmatrix} 1 & 0_{1x3} \\ 0_{3x1} & \mathcal{I}_3 - \sin(\alpha)[n^s \times] + (1 - \cos(\alpha))[n^s \times]^2 \end{bmatrix} \begin{bmatrix} 0 \\ x^s \end{bmatrix}. \tag{A-16}$$

Which is an equivalent expression to (A-6).

A-1-4   Orientation Deviations

The mapping of quaternions into an SO(3) group can be found by choosing

$$\exp_q(\bar{\eta}) = \begin{bmatrix} \cos ||\eta||_2 \\ \frac{\eta}{||\eta||_2} \sin ||\eta||_2 \end{bmatrix}, \tag{A-17}$$

which allows one to find the mapping expressed as

$$\exp_q([\eta \times]) = \mathcal{I}_3 + \sin(||\eta||_2) \left[\frac{\eta}{||\eta||_2} \times \right] + (1 - \cos(||\eta||_2) \left[\frac{\eta}{||\eta||_2} \times \right]^2. \tag{A-18}$$

The rotation quaternion can be defined as

$$q_t^{nb} = \exp_q(\frac{\bar{\eta}_t^n}{2}) \odot \tilde{q}_t^{nb}. \tag{A-19}$$

The reverse mapping can be expressed as

$$\eta = \log_q(q) = \frac{\arccos(q_0)}{||q_v||_2} q_0. \tag{A-20}$$

Finally, use can be made of approximations using the small angle theorem which are as follows

$$\exp_q(\eta) \approx \begin{bmatrix} 1 \\ \eta \end{bmatrix}, \qquad \log_q(q) \approx q_v. \tag{A-21}$$

Appendix B

B-1   Gauss-Newton Optimization

The Gauss-Newton optimization is an iterative optimization method that can be applied to non-linear equations. The Gauss-Newton optimization algorithm is suitable as a solver for a non-linear least squares problem when a good initial estimate is available and the residuals are small [50, 51]. Furthermore, the Gauss-Newton has the benefit that hessian is not computed as it is approximated using the Jacobian which in turn also guarantees positive semi-definiteness [5]. The Gauss-Newton algorithm is explained below

Consider a nonlinear measurement equation of the form

$$y = h(x) + e, \tag{B-1}$$

where y are the observations, x is the state space and $e \sim \mathcal{N}(0, \Sigma)$. The likelihood is then given by

$$p(y|x) = \frac{1}{(2\pi)^{\frac{N}{2}} \sqrt{\det(\Sigma)}} \exp\left(-\frac{1}{2}(y - h(x))^T \Sigma^{-1}(y - h(x))\right). \tag{B-2}$$

Then, under the assumption that Σ is time-invariant, the ML estimation can be found by maximizing the argument of the likelihood function,

$$\hat{x} = \arg\max_{x} p(y|x), \tag{B-3}$$

which is equivalent to minimizing the cost function $V^{NWLS(x)}$

$$\arg\min_{x} V^{NWLS}(x) = \arg\min_{x} \left((y - h(x))^T \Sigma^{-1}(y - h(x)) \right), \tag{B-4a}$$

$$\arg\min_{x} V^{NWLS}(x) = \arg\min_{x} \left(e^T(x)\Sigma^{-1}e(x) \right), \tag{B-4b}$$

The gradient $\mathcal{G}$ and Hessian $\mathcal{H}$ of the cost function $V^{NWLS}(x)$ can be calculated using the Jacobion $J(x)$. The Jacobian of the cost function is

$$J(x) = \frac{\partial e^T(x)}{\partial x} = -\frac{\partial h^T(x)}{\partial x}. \tag{B-5}$$

The gradient and Hessian are defined as

$$\underbrace{\frac{dV^{NWLS}(x)}{dx}}_{\mathcal{G}} = J(x)\Sigma^{-1}e(x), \tag{B-6a}$$

$$\underbrace{\frac{d^2V^{NWLS}(x)}{dx^2}}_{\mathcal{H}} = J(x)\Sigma^{-1}J^T(x) + \underbrace{e^T(x)\Sigma^{-1}\frac{d^2e(x)}{dx^2}}_{\approx 0}. \tag{B-6b}$$

The second term from the Hessian of the cost function can be approximated as zero under the assumption that the ML estimate of $\hat{x}$ is close enough to the true value of x. Given an initial estimate , a Gauss-Newton optimization algorithm can literately find the minimum using the following iteration

$$x^{k+1} = x^k + \mathcal{H}^{-1}\mathcal{G}, \tag{B-7a}$$

$$x^{k+1} = x^k + (J(x)\Sigma^{-1}J^T(x))^{-1}J(x)\Sigma^{-1}(y - h(x)). \tag{B-7b}$$

Appendix C

C-1 Probability Distributions

The ability to detect a change or a disturbance depends on what the Probability Density Function (PDF) looks like [47]. One of the most commonly used PDF is the normal distribution. It is also assumed in the previous Chapters that all measurements are Gaussian. The sum of multiple normally distributed variables is also normally distributed, however, summing squared normally distributed variables leads to a chi-square distribution. If the variables were zero-mean, then a central chi-square distribution forms, however, if the variables were not zero-mean than a non-central chi-square distribution forms. The different distributions are shown below.

C-1-1 Normal Distribution

The normal distribution also known as the Gaussian distribution is denoted by

$$X \sim \mathcal{N}(\mu, \sigma^2), \tag{C-1}$$

where X is the random stochastic variable, μ is the mean value and σ^2 is the variance. The PDF is shown in Figure C-1 and is defined as

$$f_X(x) = \frac{1}{\sqrt{2\pi\sigma^2}} \exp\left(-\frac{1}{2\sigma^2}(x-\mu)^2\right), \quad -\infty < x < \infty. \tag{C-2}$$

The probability of X falling in between an interval $[a, b]$ can be found by taking the integral from a to b as

$$P(a \leq X \leq b) = \int_a^b f_X(x)dx. \tag{C-3}$$

The scalar case in (C-2) can be extended into a vector such that X becomes of length n. Giving rise to the more general formulation

$$f_X(x) = \frac{1}{(2\pi)^{\frac{n}{2}}\sqrt{\det(Q)}} \exp\left(-\frac{1}{2}(x-\mu)^T Q^{-1}(x-\mu)\right), \quad -\infty < x < \infty. \tag{C-4}$$
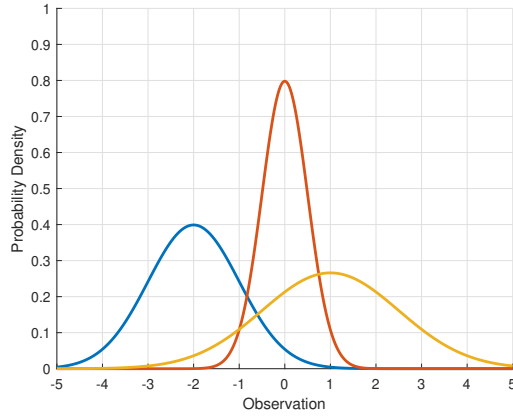
Figure C-1: Normal Probability Density Function for varying μ and σ^2.

C-1-2 Chi-square distributions

The Chi-square distribution arises when the sum is taken of squared normally distributed variables X_i which are also Independent and Identically Distributed (IID) [47], i.e. $Y = \sum_{i=1}^{\nu} X_i^2$. If $X - i$ has zero mean then one gets the central Chi-square distribution, if they have non-zero mean one gets the noncentral Chi-square distribution.

Central Chi-square distribution If the squared variables happen to have zero-mean, i.e. $X_i \sim \mathcal{N}(0, Q)$, then a central Chi-square distribution $Y \sim \chi_\nu^2$ is formed. The degrees of freedom, denoted by ν is assumed to be a positive integer [47] can be seen as how many IID squared variables are summed and as ν goes to infinity the Chi-square distribution goes towards the Normal distribution.

The probability density function is strictly positive and takes the form of

$$f_X(x) = \begin{cases} \frac{1}{2^{\frac{\nu}{2}} \Gamma\left(\frac{\nu}{2}\right)} x^{\frac{\nu}{2}-1} e^{-\frac{1}{2}x} & x > 0, \\ 0 & x < 0, \end{cases} \tag{C-5}$$

where $\Gamma(u)$, also known as the Gamma function, is defined as

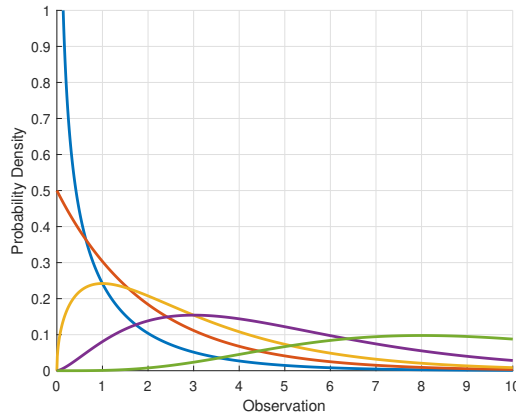$$\Gamma(u) = \int_0^\infty t^{u-1} e^{-t}. \tag{C-6}$$

Figure C-2: Central Chi-square Probability Density Function for varying ν.

Non-central Chi-square distribution If, however, the variables has non-zero mean, i.e. $X_i \sim \mathcal{N}(\mu_i, Q)$ then a Non-central Chi-square distribution $Y \sim \chi_\nu^2(\lambda)$ is formed. Where λ is defined as the noncentrality parameter $\lambda = \sum_{i=1}^{\nu} \mu_i^2$. When $\lambda = 0$ the non-central Chi-square distribution takes shape of the central Chi-square distribution [47].

Again, the probability density function is strictly positive but now takes the shape of

$$p(x) = \begin{cases} \frac{1}{2}\left(\frac{x}{\lambda}\right)^{\frac{\nu-2}{4}} I_{\frac{\nu}{2}-1}(\sqrt{\lambda x})\exp\left(-\frac{1}{2}(x+\lambda)\right) & x > 0, \\ 0 & x < 0, \end{cases} \tag{C-7}$$

where $I_r(u)$ is defined as

$$I_r(u) = \frac{\left(\frac{1}{2}u\right)^r}{\sqrt{\pi}\Gamma\left(r+\frac{1}{2}\right)}\int_0^\pi \sin^{2r}(\theta)e^{u\cos\theta}d\theta. \tag{C-8}$$
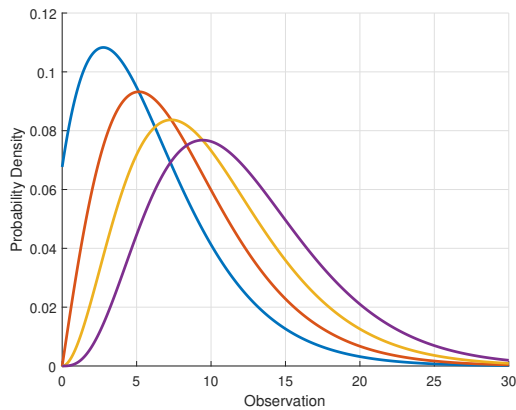

Figure C-3: Non-central Chi-square Probability Density Function for varying ν.

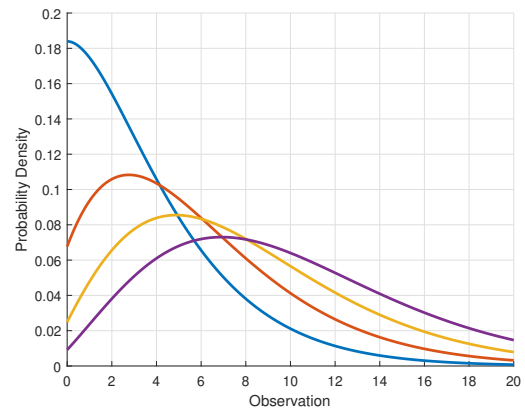**Figure C-4:** Non-central Chi-square Probability Density Function for varying λ.

$$\text{Appendix } D$$

Appendix D

D-1   Biases, covariance of array
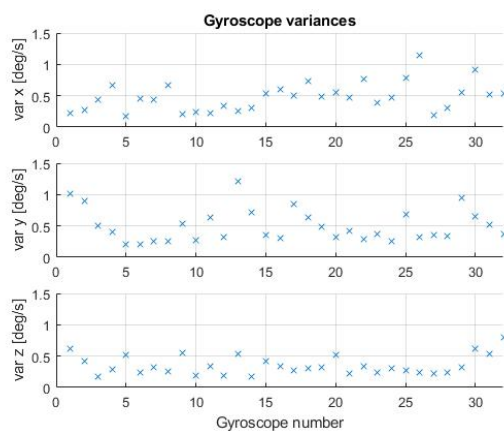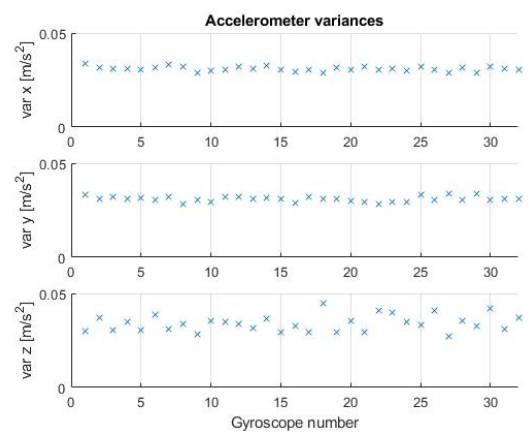

Figure D-1

Figure D-2
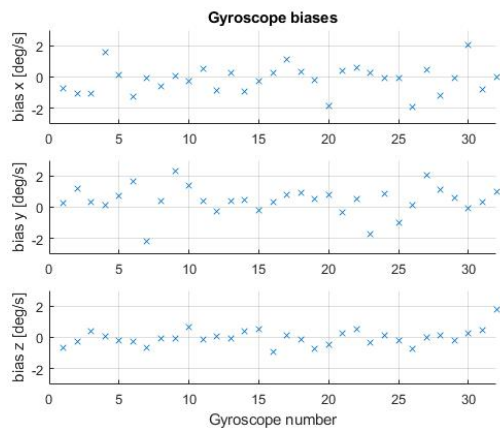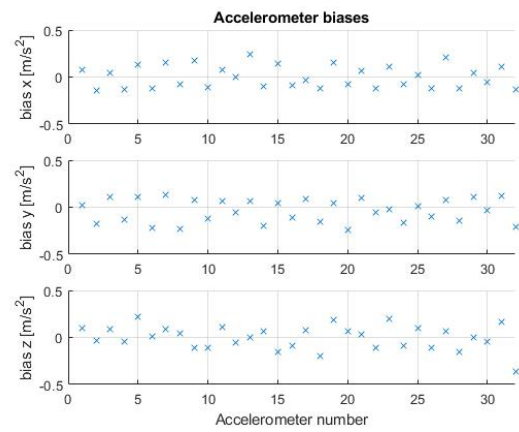
Figure D-3

Figure D-4

Appendix E

Appendix E

E-1   Algorithm for data generation of Multiple IMUs

Algorithm 6: Simulation of rigid body motion to generate accelerometer and gyroscopes measurement data.

Set $g^n = \begin{bmatrix} 0 & 0 & 9.81 \end{bmatrix}^T$ and initial condition $q_0 = \begin{bmatrix} 1 & 0 & 0 & 0 \end{bmatrix}^T$;

Assign values for $a^b_{1:N}$, $\omega^b_{1:N+1}$, $b_{a,1:N_a}$ and $b_{\omega,1:N_\omega}$;

for $k = 1 : N$ **do**

  Calculate the angular acceleration;

  $$\dot{\omega}^b_k = \frac{\omega^b_{k+1} - \omega^b_k}{T}.$$

  Update quaternion, ;

  $$q^{nb}_k = \exp_q(\frac{\omega^b_k}{2}) \odot q^{nb}_{k-1},$$

  Find rotation matrix ;

  $$R^{bn}_k = \left[q_v q_v^T + q_0^2 \mathcal{I}_3 + 2q_0 [q_v \times] + [q_v \times]^2 \right].$$

  Ω^b_k is constant for every accelerometer;

  $$\Omega^b_k = \left([\omega^b_k \times]^2 + [\dot{\omega}^b_k \times] \right).$$

  Set accelerometer measurements;

  for $i = 1 : N_a$ **do**

    $$y_{a_i,k} = R^{s_i b} \left(\left(a^b_k - R^{bn}_k g^n \right) + \Omega^b_k \rho_i \right) + b^{s_i}_{a_i} + e^{s_i}_{a_i,k}.$$

  end

  Set gyroscope measurements;

  for $j = 1 : N_\omega$ **do**

$$y_{\omega_j,k} = R^{s_j b} \omega^b_k + b^{s_j}_{\omega,j} + e^{s_j}_{\omega_j,k}.$$

  end

end

E-2 Additional Results on the covariance of the specific force, angular velocity and angular acceleration of the MIMU4844 array

E-2-1 Varying number of gyroscopes

For this simulation 32 accelerometers, 1 to 32 gyroscopes with the standard array configuration
at $\omega = \begin{bmatrix} 10 & 10 & 10 \end{bmatrix}^T rad/s$ was simulated. The results are plotted in Figure E-1.

Angular velocity   As expected the covariance of the angular velocity decreases with N_ω. It
can be observed that the

Angular acceleration   The covariance angular acceleration is not impacted by the number
of gyroscopes, which is as expected.

Specific force   Similarly to the angular acceleration, the specific force covariance is not
impacted by adding more gyroscopes.

waarschijnlijk komt die omdat niet alle covariances hetzelfde zijn bij de CLRB, en bij mean is het gemiddelde genomemn van alles
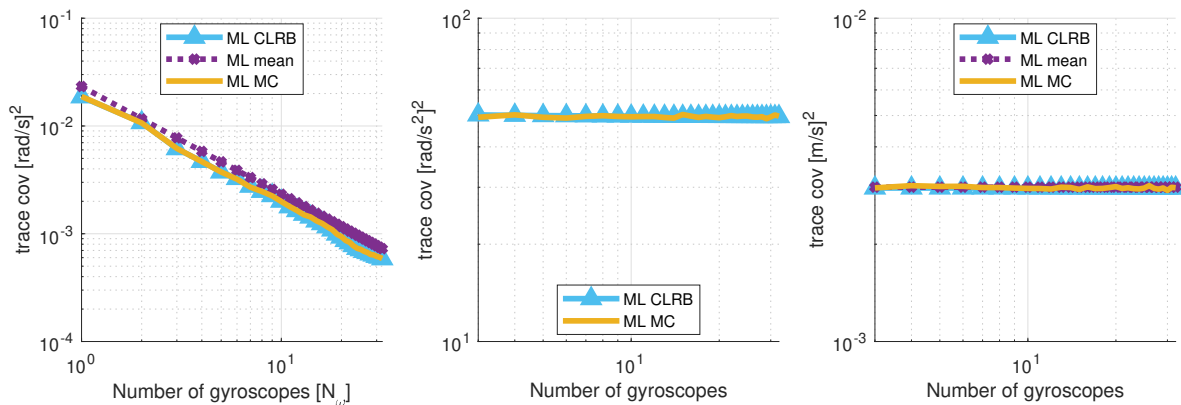

Figure E-1: Angular velocity covariance (left) Angular acceleration covariance (mid) and Specific
force covariance (right) plotted against number of gyroscopes N_ω. All 32 accelerometers were
used and the angular velocity was set at $\omega = \begin{bmatrix} 10 & 10 & 10 \end{bmatrix}^T rad/s$. The IMU locations are based
on a real IMU array also shown in Figure 4-1

Bibliography

[1] "Xsens Technologies B.V.," 2016. Accessed on 2020 September 29.

[2] "Inertial Elements," 2016. Accessed on 2020 September 30.

[3] J. O. Nilsson and I. Skog, "Inertial sensor arrays - A literature review," in *2016 European Navigation Conference, ENC 2016*, Institute of Electrical and Electronics Engineers Inc., 8 2016.

[4] C. M. Brigante, N. Abbate, A. Basile, A. C. Faulisi, and S. Sessa, "Towards miniaturization of a MEMS-based wearable motion capture system," *IEEE Transactions on Industrial Electronics*, vol. 58, no. 8, pp. 3234–3241, 2011.

[5] M. Kok, J. D. Hol, and T. B. Schön, "Using inertial sensors for position and orientation estimation," *Foundations and Trends in Signal Processing*, vol. 11, no. 1-2, pp. 1–153, 2017.

[6] S. Guerrier, D. J. Skaloud, and A. Wägli, "Integration of Skew-Redundant MEMS-IMU with GPS for Improved Navigation Performance," Tech. Rep. February 2015, 2008.

[7] S. Sun, X. Meng, L. Ji, Z. Huang, and J. Wu, "Adaptive Kalman filter for orientation estimation in micro-sensor motion capture," *Fusion 2011 - 14th International Conference on Information Fusion*, 2011.

[8] Y. Y. Shen and A. P. Anderson, "Extended Kalman Filter for Magnetometer-Free Estimation of Spacesuit Wearer Joint Kinematics Using Inertial Measurements," tech. rep., 2019.

[9] M. Perlmutter and L. Robin, "High-performance, low cost inertial MEMS: A market in motion!," pp. 3–7.

[10] O. J. Woodman, "Number 696 An introduction to inertial navigation An introduction to inertial navigation," 2007.

[11] G. Panahandeh, I. Skog, and M. Jansson, "Calibration of the accelerometer triad of an inertial measurement unit, maximum likelihood estimation and Cramér-Rao bound," in *2010 International Conference on Indoor Positioning and Indoor Navigation, IPIN 2010 - Conference Proceedings*, 2010.

[12] D. K. Shaeffer, "MEMS inertial sensors: A tutorial overview," *IEEE Communications Magazine*, vol. 51, no. 4, pp. 100–109, 2013.

[13] H. Carlsson, I. Skog, and J. Jaldén, "On-the-fly geometric calibration of inertial sensor arrays," *2017 International Conference on Indoor Positioning and Indoor Navigation, IPIN 2017*, vol. 2017-Janua, no. September, pp. 1–6, 2017.

[14] I. Skog, J. O. Nilsson, P. Handel, and A. Nehorai, "Inertial Sensor Arrays, Maximum Likelihood, and Cramér-Rao Bound," *IEEE Transactions on Signal Processing*, vol. 64, pp. 4218–4227, 9 2016.

[15] P. Cardou and J. Angeles, "Angular velocity estimation from the angular acceleration matrix," *Journal of Applied Mechanics, Transactions ASME*, vol. 75, pp. 0210031–0210038, 3 2008.

[16] J. Wahlström, I. Skog, and P. Händel, "Inertial Sensor Array Processing with Motion Models," *2018 21st International Conference on Information Fusion, FUSION 2018*, pp. 788–793, 2018.

[17] P. G. Savage, "Strapdown inertial navigation integration algorithm design part 1: Attitude algorithms," *Journal of Guidance, Control, and Dynamics*, vol. 21, no. 1, pp. 19–28, 1998.

[18] G. D. Catalunya, "Redundant Imus for Precise Trajectory Determination," tech. rep., 2004.

[19] N. El-Sheimy and X. Niu, "The Promise of MEMS to the Navigation Community," *Inside GNSS*, pp. 46–56, 2007.

[20] S. Guerrier, "Improving accuracy with multiple sensors: Study of redundant MEMS-IMU/GPS configurations," tech. rep., 2009.

[21] Ryan Hanson, "Using Multiple MEMS IMUs to form a Distributed Inertial Measurement Unit," tech. rep., 2005.

[22] M. STURZA, "Skewed axis inertial sensor geometry for optimal performance," American Institute of Aeronautics and Astronautics (AIAA), 10 1988.

[23] A. Waegli, S. Guerrier, and J. Skaloud, "Redundant MEMS-IMU integrated with GPS for performance assessment in sports," tech. rep., 2008.

[24] S. Sukkarieh, P. Gibbens, B. Grocholsky, K. Willis, and H. F. Durrant-Whyte, "A low-cost, redundant inertial measurement unit for unmanned air vehicles," *International Journal of Robotics Research*, vol. 19, pp. 1089–1103, 11 2000.

[25] J. J. Gertler, *Fault detection and diagnosis in engineering systems.* 2017.

[26] E. Gagnon, A. Vachon, and Y. Beaudoin, "Data fusion architectures for orthogonal redundant inertial measurement units," *Sensors (Switzerland)*, vol. 18, no. 6, 2018.

[27] A. Waegli, J. Skaloud, S. Guerrier, M. E. Parés, and I. Colomina, "Noise reduction and estimation in multiple micro-electro-mechanical inertial systems," *Measurement Science and Technology*, vol. 21, no. 6, 2010.

[28] J. B. Bancroft and G. Lachapelle, "Data fusion algorithms for multiple inertial measurement units," *Sensors*, vol. 11, pp. 6771–6798, 7 2011.

[29] H. A. Hashim, "Special Orthogonal Group SO(3), Euler Angles, Angle-axis, Rodriguez Vector and Unit-Quaternion: Overview, Mapping and Challenges," no. 3, 2019.

[30] R. Bhat, R. Dukkipati, and M. Pascal, *Advanced Dynamics*, vol. 55. Cambridge University Press, 2002.

[31] M. Verhaegen and V. Verdult, *Filtering and system identification: A least squares approach*, vol. 9780521875. Cambridge university press, 2007.

[32] M. E. Pittelkau, "Calibration and attitude determination with Redundant Inertial Measurement Units," *Journal of Guidance, Control, and Dynamics*, vol. 28, no. 4, pp. 743–752, 2005.

[33] F. L. Markley, "Attitude error representations for Kalman filtering," *Journal of Guidance, Control, and Dynamics*, vol. 26, no. 2, pp. 311–317, 2003.

[34] T. Forsberg, N. Grip, and N. Sabourova, "Non-iterative calibration for accelerometers with three non-orthogonal axes, reliable measurement setups and simple supplementary equipment," *Measurement Science and Technology*, vol. 24, no. 3, 2013.

[35] F. Olsson, M. Kok, K. Halvorsen, and T. B. Schon, "Accelerometer calibration using sensor fusion with a gyroscope," in *IEEE Workshop on Statistical Signal Processing Proceedings*, vol. 2016-Augus, IEEE Computer Society, 8 2016.

[36] U. Qureshi and F. Golnaraghi, "An Algorithm for the In-Field Calibration of a MEMS IMU," *IEEE Sensors Journal*, vol. 17, no. 22, pp. 7479–7486, 2017.

[37] M. Kok and T. B. Schon, "Magnetometer calibration using inertial sensors," *IEEE Sensors Journal*, vol. 16, pp. 5679–5689, 7 2016.

[38] W. Cheney and D. Kincaid, "Linear Algebra: Theory and Applications," p. 624, 2010.

[39] Z. Lin, Q. Zou, E. S. Ward, and R. J. Ober, "Cramer-Rao lower bound for parameter estimation in nonlinear systems," *IEEE Signal Processing Letters*, vol. 12, pp. 855–858, 12 2005.

[40] J. Chaffee and J. Abel, "GDOP and the Cramer-Rao bound," in *Record - IEEE PLANS, Position Location and Navigation Symposium*, pp. 663–668, Publ by IEEE, 1994.

[41] F. Gustafsson, *Statistical Sensor Fusion*. 2013.

[42] A. G. Jaffer, "Maximum Likelihood Direction Finding of Stochastic Sources: a Separable Solution.," in *ICASSP, IEEE International Conference on Acoustics, Speech and Signal Processing - Proceedings*, pp. 2893–2896, IEEE, 1988.

[43] Y. Bresler, "Maximum likelihood estimation of a linearly structured covariance with application to antenna array processing," pp. 172–175, Publ by IEEE, 1988.

[44] P. Stoica and A. Nehorai, "On the concentrated stochastic likelihood function in array signal processing," Tech. Rep. 5, 1995.

[45] D. Törnqvist, "Statistical Fault Detection with Applications to IMU Disturbances," 2006.

[46] R. Christensen, "Testing fisher, neyman, pearson, and bayes," *American Statistician*, vol. 59, pp. 121–126, 5 2005.

[47] S. K. Sengupta and S. M. Kay, *Fundamentals of Statistical Signal Processing: Estimation Theory*, vol. 37. Upper Saddle River, NJ, USA: Prentice-Hall, Inc., 1995.

[48] D. Törnqvist, F. Gustafsson, and I. Klein, "GLR tests for fault detection over sliding data windows," *IFAC Proceedings Volumes (IFAC-PapersOnline)*, vol. 16, pp. 743–748, 1 2005.

[49] D. Törnqvist and F. Gustafsson, "Eliminating the initial state for the generalized likelihood ratio test," *IFAC Proceedings Volumes (IFAC-PapersOnline)*, vol. 6, pp. 599–604, 1 2006.

[50] P. E. Gill and W. Murray, "Algorithms for the Solution of the Nonlinear Least-Squares Problem," *SIAM Journal on Numerical Analysis*, vol. 15, pp. 977–992, 10 1978.

[51] S. HILOUT, "GaussNewton method," *Numerical Methods for Equations and its Applications*, pp. 220–251, 2012.

Glossary

List of Acronyms

IMUs	Inertial Measurement Units
MEMS	Micro-Electromechanical System
KF	Kalman Filter
EKF	Extended Kalman Filter
MEKF	Multiplicative Extended Kalman Filter
ML	Maximum Likelihood
MAP	Maximum A Posteriori
CRLB	Cramér-Rao Lower Bound
FDI	Fault Detection and Isolation
IID	Independent and Identically Distributed
GLRT	Generalised Likelihood Ratio Test
MLRT	Marginalised Likelihood Ratio Test
FIM	Fisher Information Matrix
SLS	Separable Least Squares
PDF	Probability Density Function